Development and assessment of broadband surface albedo from Clouds and the Earth's Radiant Energy System Clouds and Radiation Swath data product

David Rutan,[1] Fred Rose,[1] Miguel Roman,[2] Natividad Manalo-Smith,[1] Crystal Schaaf,[2] and Tom Charlock[3]

[1]   We describe a method to determine broadband albedo globally over land viewed by the Clouds and the Earth's Radiant Energy System (CERES) scanning radiometers on board the TRMM, Terra, and Aqua satellites. This albedo is used as a surface boundary condition for a fast radiation transfer code in the Surface and Atmospheric Radiation Budget (SARB) subsystem of the CERES processing scheme. Cloudy sky surface albedo is estimated from derived clear sky values. Clear sky surface albedo is assessed by comparing the CERES/SARB-based surface albedo with the bidirectional reflectance distribution function (BRDF)–based surface albedo supplied by the MODIS land surfaces group. The SARB method employs broadband observations at the top of atmosphere (TOA) and assumes relative spectral shape of surface albedo. The MODIS group uses higher spatial resolution observations in several shortwave window channels to retrieve spectral surface albedos and then scales up to broadband surface albedo. Comparisons over snow-free land show good agreement between the two independent products on the scale of the CERES footprint. Biases run approximately 0.005 absolute or 0.02 relative with SARB albedo, generally lower than MODIS. We find little dependence on view geometry and slight functional dependence on aerosol optical depth. The value selected for a priori surface spectral albedo is important, but not critical, when retrieving broadband surface albedo with broadband TOA data. However, based on calculations, aerosol forcing to TOA flux changes in spectral albedo shape can affect aerosol forcing for as much as would a 15% absolute change in the original broadband surface albedo.

1. Introduction

[2]   Clouds and the Earth's Radiant Energy System (CERES) instruments [*Wielicki et al.*, 1996] on NASA's Tropical Rainfall Measurement Mission (TRMM), and Earth Observing System (EOS) Terra and Aqua satellites measure broadband shortwave and longwave energy reflected and emitted at the Top of the Atmosphere (TOA) as a follow on to the NASA Earth Radiation Budget Experiment (ERBE [*Barkstrom and Smith*, 1986]). CERES however goes beyond ERBE with advanced data products that synthesize broadband observations with other EOS data streams. One such product is the Clouds and Radiation Swath (CRS) developed by the CERES Surface and Atmo-

spheric Radiation Budget (SARB) working group [*Charlock et al.*, 1997, 2006]. SARB runs a fast radiation transfer calculation whose location is dictated by the CERES field of view. The TRMM satellite is in a precessing orbit of 36°; it observes the tropics and midlatitudes at varying times of day. Terra and Aqua are in sun-synchronous orbits, and so view all latitudes. These orbits and the viewing capabilities of CERES and other instruments on board enable surface albedo estimates for the entire globe and for different times of day.

[3]   Broadband surface albedo is generally defined as the ratio of shortwave solar irradiance (generally between ∼0.2 μm and 4.0 μm) reflected by a surface to the irradiance impinging on that same surface. Since incoming irradiance is dependent on atmospheric state, reflected irradiance is dependent upon surface properties, and both change over time, surface albedo is then clearly a continuously varying function of atmospheric and surface conditions. Hence the accuracy of a retrieval method for broadband surface albedo depends upon an accurate description of the atmosphere and the reflective properties of a surface over time. The goal of this paper is to describe

[1]Science Systems and Applications, Inc., Hampton, Virginia, USA.
[2]Department of Geography, Center for Remote Sensing, Boston University, Boston, Massachusetts, USA.
[3]Science Directorate, NASA Langley Research Center, Hampton, Virginia, USA.

methodologies developed to accomplish this task for the field of view of CERES instruments and evaluate the resulting clear sky spectral and broadband estimates against independent observations.

[4] The accurate determination of surface albedo on a global scale is also important because of concerns regarding anthropogenic changes to the environment and its effects on radiation balance. With the advent of NASA's Earth Observing System satellites the enhanced observations of EOS make it possible to retrieve surface albedo with more confidence; one goal, for example, is estimating the radiative forcing effect of surface albedo due to changes in land cover. Radiative forcing due to anthropogenic changes to global surface albedo is addressed in the 4th IPCC report AR4-WG1-Chapter 2.5 [*Forster et al.*, 2007]. There the authors describe radiative forcing from surface albedo (reflecting land cover changes since 1750) is generally on the order of -0.1 W m^{-2} to -0.2 W m^{-2} globally [*Forster et al.*, 2007]. This is a near balance of obviously large local changes of opposing sign. CERES has the advantage of being a broadband instrument, viewing the majority of the shortwave spectrum, thus potentially giving excellent estimates of broadband surface albedo at CERES footprint time and space scales. The CERES/SARB algorithm described and assessed in this paper supplies a surface albedo that has a nominal spatial scale of ∼30 km at the Earth's surface. In "downstream" CERES data products, a similar algorithm is run for grid box means to give global, gridded surface albedo estimates. These later CERES data products can better assess the impact of global surface albedo on radiative forcing. Here we focus on methodology and assessment of the surface albedos used to run the SARB radiation transfer model on a footprint-by-footprint basis and include a section on the connection between surface albedo and aerosol forcing to the shortwave flux at the top of the atmosphere.

[5] In this paper we consider data from EOS Terra Flight Model 1 (FM1) and Flight Model 2 (FM2) CERES instruments and the radiation transfer model used in calculating the profile of irradiance beneath CERES observations. Methodology for the other CERES instrument data streams is the same. We pay particular attention to the method of defining surface characteristics observed beneath CERES footprints. Resulting surface albedos are compared to surface observations, but these point measurements are generally inadequate for validation of surface albedos determined under the large footprints, except for unusually homogeneous sites. Subsequently we use surface albedo derived by the MODerate resolution Imaging Spectroradiometer (MODIS) instrument on board Terra to assess SARB albedos. This data product originates from narrow band channels of the MODIS instrument. The algorithm is based on establishing a theoretical BRDF every eight days [*Lucht et al.*, 2000b; *Schaaf et al.*, 2002] and has produced valuable new data sets that provide both spectral albedo in the MODIS channels and estimates of broadband albedo at a number of spatial and temporal scales. To assess the SARB albedo, MODIS albedos are closely matched in space and time and then integrated within the field of view of the CERES instrument where we find a close agreement between broadband surface albedo from these two nearly independent sources.

[6] We use the most currently available, respective generations of retrievals for surface albedo from MODIS and CERES that are matched in time. The MODIS Land Team uses Terra Collection 5 MODIS radiances as its source. The SARB albedos presented are from CERES CRS Edition 2B data product, which includes inputs based on the earlier generation of Terra Collection 4 MODIS radiances. For the next few years, the analyst seeking several years of concurrent surface albedos from both MODIS and CERES would likely employ the respective generations of MODIS and CERES used here. CERES CRS albedos using Collection 5 of MODIS have not yet been released. The CRS data product used here can be overwhelming due to the CERES sampling rate. The CERES Time Interpolation Spatial Averaging (TISA) working group takes CRS footprint surface albedo and averages them over the globe into a monthly, $1 \times 1°$ grid, at the CERES overpass times. These maps, which may be more convenient than footprint data, depending on one's application, are found at the CERES/ARM Validation Experiment (CAVE) home page (http://www-cave.larc.nasa.gov/cave/fsw-sfcalb/).

2. Clouds and Earth's Radiant Energy System (CERES)

2.1. CERES Instruments

[7] CERES instruments measure broadband radiance in three channels, shortwave (SW) reflected (mostly from 0.2 μm to 4.0 μm), "total broadband" (mostly 0.2 μm to 100.0 μm), and in the window range of ∼8.0 μm to 12.0 μm. Longwave (LW) emitted radiation (mostly 4.0 μm to 100.0 μm) is inferred as the difference between the total and SW channels. CERES Preflight Model (PFM) operated for 8 months on board the TRMM satellite in 1998. Four other CERES instruments are currently on board EOS satellites, FM1 and FM2 onboard Terra, and on Aqua, Flight Models 3 and 4 (FM3 and FM4). The data rate of the CERES instruments is 100 footprints per second. Spatially the footprint size is variable depending on satellite altitude and instrument view angle. The shape of the CERES aperture and the response of the instrument in terms of energy detected, assuming a 95% response, convolve to an approximate 31 km × 30 km area at the surface of the Earth for a nadir view for the Terra footprint [*Green and Wielicki*, 1997, Table 4.4-1]. In this paper we utilize CERES Terra FM1 and FM2 observations in cross-track mode.

[8] Because direct measurements of irradiance upwelling to a satellite can represent the ERB accurately at only very course time and space scales [*Smith and Green*, 1981], it is preferable to scan for radiance and infer irradiance by applying scene-dependent, empirically based statistical models [*Suttles et al.*, 1988]. CERES surpasses ERBE in this regard, both by inferring the scene from high resolution MODIS data [*Minnis et al.*, 2003] and by applying fairly robust angular distribution models (ADMs [*Loeb et al.*, 2005]) founded on the complex CERES rotating azimuth plane scan (RAPS) mode to establish BRDF on the scale of ∼30 km broadband footprints; no other EOS instrument can employ RAPS to buttress the products of its routine cross-track scan. The error due to this inversion cannot be known for any single CERES footprint but it can be estimated for groups of footprints [*Loeb et al.*, 2005, 2007]. Its effect

however will be inherent in our derivation of surface albedo. After computing aggregate estimates of root mean square error as a function of scene type, *Loeb et al.* [2007] gives the rough estimate of a TOA SW error due to inversion using ADMs of approximately 5% due to surface scene type. This estimate will be used later in a sensitivity table to analyze its effect on our estimate of broadband surface albedo. Land surface albedo is inferred from a cloud screened set of these measurements and the radiative transfer code described in the next section; the code is comparable to those used in some Global Climate Models (GCMs). The CERES derived land albedo presented here constitutes a surface boundary condition for climate models that is consistent with the ERB observations that are often used to validate the climate models at TOA.

2.2. CERES: Surface and Atmospheric Radiation Budget (SARB)

[9] Within the CERES science team SARB group is tasked with calculating vertical profiles of heating rates, globally, and continuously beneath CERES footprint observations of TOA fluxes [*Charlock et al.*, 1997, 2006]. This is accomplished using a fast radiation transfer code originally developed by *Fu and Liou* [1993] and subsequently modified by the SARB team [*Kato et al.*, 2005; *Rose and Charlock*, 2002]; hereafter referred to as *Langley Fu and Liou 2005* or (LFL05). The baseline data product for the SARB subsystem is the Clouds and Radiative Swath (CRS). Each CRS file contains one hour of CERES footprint data and includes CERES TOA observed radiances and fluxes and an analyses of those MODIS pixels collocated within the larger CERES footprint, which supply cloud properties inside the footprint. Along with CERES TOA fluxes and cloud analyses, CRS files include column fluxes at five atmospheric pressure levels (Surface, 500 hPa, 200 hPa, 70 hPa, and TOA). These fluxes are a subset of the radiation transfer calculations, which are executed at higher vertical resolutions. A key input for SW calculations is spectral surface albedo under all sky conditions and for any location on the globe.

2.3. SARB: Radiation Transfer Model and Model Input

[10] The SW portion of the LFL05 model is a delta-two-stream radiation transfer code with fifteen spectral bands from 0.175 μm to 4.0 μm. Cloud optical properties within the CERES field of view are defined in a separate CERES data product, the Single Satellite Flux (SSF) product. In the SSF, MODIS imager pixels are collocated within the larger CERES footprint and weighted by the energy distribution of the CERES instrument. From these MODIS values, cloud properties, including cloud fraction [*Minnis et al.*, 2003, 2004] are derived and used as input for the radiation transfer model. The only cloud product used in this paper is the cloud mask. Aerosol optical depths are input from MODIS (MOD08D3) product [*Remer et al.*, 2005]. When lacking the instantaneous MOD08D3 product in a CERES footprint, the first alternate is the daily, gridded MOD04, and the second is the Model for Atmospheric Transport and CHemistry (MATCH [*Collins et al.*, 2001]), supplied courtesy of Dr. David Fillmore at NCAR, Boulder, CO. MATCH is a global aerosol model that assimilates MODIS retrievals of AOD. The MATCH model is also used to define aerosol constituents (using Optical Properties of Aerosol and Clouds, OPAC) optical properties from *Hess et al.* [1998], and an update to *Tegen and Lacis* [1996], desert dust properties supplied courtesy of Dr. Andrew Lacis of GISS, and places aerosols throughout the vertical atmospheric column. Pressure, temperature, and water vapor profiles are specified from GEOS-4.0 [*Bloom et al.*, 2005], a 1° gridded reanalysis data product from Goddard Modeling Assimilation Office. Ozone comes from the National Center for Environmental Prediction, Stratospheric Monitoring Group Ozone Blended Analysis (SMOBA) product [*Yang et al.*, 2000]. The radiation transfer model, LFL05, is typically run for CERES footprints in which MODIS cloud properties have been derived (∼2 million per day) using up to 36 atmospheric levels.

3. Determination of Surface Albedo

3.1. Estimating Broadband Surface Albedo From CERES Observations

[11] As described above LFL05 currently models 15 spectral intervals (shown in Figure 1) between 0.17 μm and 4.0 μm in the shortwave spectrum. For each daytime CERES observation where LFL05 is run, both a surface scene-dependent albedo spectral shape and an initial estimate of broadband surface albedo are required for the broader SARB operation. We now describe how these are retrieved for clear CERES footprints. To determine these values the code uses a logic sequence based on scene type determined by MODIS imager pixels collocated within the larger CERES footprint and a fixed 1/6° equal angle resolution global surface scene type map discussed below. After scene type is determined the algorithm utilizes look-up tables (LUT), based on radiation transfer models, to estimate an initial broadband albedo α_{clr} that is consistent with the observed broadband albedo at TOA. The full LFL05 radiative transfer code is not run at the footprint scale for this first step. This initial estimate is similar to previous methodologies for determining surface albedo [*Gupta et al.*, 2001; *Pinker and Laszlo*, 1992; *Rutan et al.*, 2006]. For land, snow and ice surfaces under clear skies, the LUT is based on a parameterization of LFL05 itself. Model dependencies are shown in equation (1).

$$\alpha_{clr} = LUT\{\alpha_{TOA}, \mu, \tau_{aod}, \omega_{aod}, T_{aod}, pw, P_{sfc}, O_3, T_{sfc}\} \quad (1)$$

[12] Inputs to the LUT include CERES observed TOA albedo (α_{TOA}), cosine solar zenith angle μ, aerosol optical depth τ_{aod}, one minus aerosol single scatter albedo (ω_{aod}), aerosol type T_{aod}, column precipitable water (pw), surface pressure (P_{sfc}), ozone (O_3), and a coarse initial spectral shape parameter, T_{sfc} defined as ln(A_{vis}/A_{nir}) where A_{vis} and A_{nir} are bands 11 (0.5–0.7 μm) and 12 (0.7–1.3 μm) as shown in Figure 1 and whose determination is based on observed scene types as described in section 3.2.

[13] Equation (1) describes a LUT that is required to determine clear sky surface albedo globally under a broad range of meteorological conditions from high altitude, dry regimes such as the Antarctic plateau to moist tropical forests to bright deserts. To give an idea of the impact on the LUT to most inputs a simple sensitivity study is shown
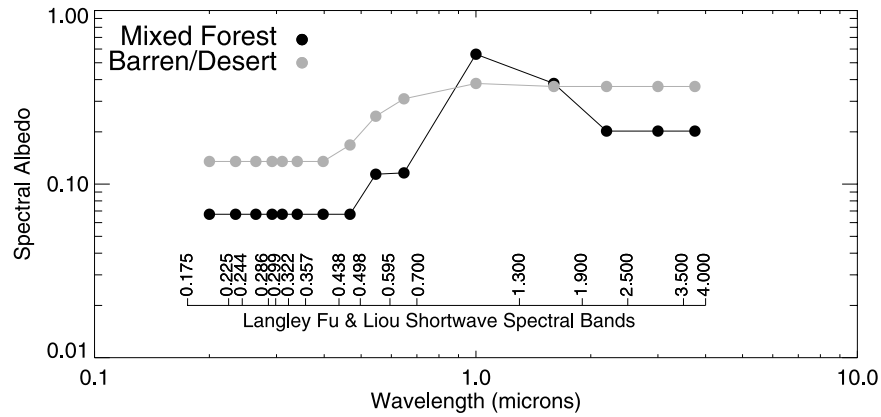
Figure 1. Shortwave spectral bands used in LFL05 radiation transfer model and associated spectral albedo used in CRS processing for IGBP scene types, mixed forest and barren desert.

in Tables 1 and 2. There we chose a base state atmosphere shown in the top row and fixed cosine solar zenith angle of 0.5 for all runs. Next each of the remaining seven input variables are modified lower, then higher, one at a time holding the other base state variables to their original values. Table 1 shows that for most vegetated scenes the LUT is most sensitive to aerosol optical depth, precipitable water and TOA albedo. For brighter scenes, Table 2 shows the LUT is more sensitive to precipitable water, TOA albedo, and aerosol single scatter albedo.

[14] The surface albedo of water (free of sea ice) is not retrieved using equation (1). Instead, it is specified from a LUT based on the Coupled Ocean Atmosphere Radiation Transfer (COART) [*Jin et al.*, 2004]. This LUT has inputs of solar zenith angle, wind speed, aerosol optical depth and chlorophyll concentration. Solar zenith angle comes from CERES ephemeris data and aerosol optical depth and wind speed are available from the same products described for SARB radiation transfer described briefly above in section 2.3. Global chlorophyll data products were not available when CERES CRS Edition 2B was begun and so chlorophyll is set to a constant of 0.1 mg/m³.

3.2. Estimating Albedo Spectral Shape for 15 LFL05 SW Bands

[15] We now address the derivation of albedo spectral shape across the required 15 LFL05 SW bands as shown in Figure 1. Because global data sets of spectral albedos were not available in the time for the full stream of CERES processing, albedo spectral shape was estimated by another route. For snow and sea ice scenes, a LUT based on a specialized COART model with surface snow grains [*Jin et al.*, 1994, 2008] gives albedo spectral shape. Both the CERES cloud algorithm and daily microwave maps from

NSIDC and NOAA identify snow and ice. For non–snow land scenes the SARB algorithm depends upon associating predefined spectral albedos to a global surface scene type map developed from the 1 km resolution map International Geosphere Biosphere Programme (IGBP) scene types available from the United States Geological Survey (USGS) at http://eros.usgs.gov/products/landcover/glcc.php. We add an 18th type, ''Tundra'', to distinguish high altitude and high latitude desert scenes by folding in the Global Ecosystem Map, available from the same USGS web site listed above. Where IGBP identifies ''barren'' and the Global Ecosystems map identifies ''tundra'' we change the IGBP type to ''tundra.''

[16] To create the operational surface scene type map, we decrease the spatial resolution of the USGS IGBP map in the following manner. Each 1 km IGBP type is assigned a spectral albedo from the literature or field experiments as listed in Table 3. These spectral albedos readily supply a simple fixed broadband albedo for the 18 IGBP scene types. The 1 km broadband surface albedos are integrated over 10-minute (1/6°) equal angle grid boxes. The resulting average is compared to the list of 18 scene type based values and the closest matching IGBP type yields the albedo spectral shape that will represent that particular 10' grid box. An alternative might be to simply histogram IGBP types within each 10-minute box; but with such a method the integrated energy of the scene is potentially lost; and as we are less concerned with actual vegetation type and more concerned with approximating the amount of radiation reflected within a given 10' box, we use the former method.

[17] A further intricacy arises in the selection of albedo spectral shape because of the convention for placement of IGBP scene types within CERES footprints. The CERES data stream allows for up to eight surface types to be

Table 1. Surface Albedo LUT Model Sensitivity to Various Input Variables[a] With Initial TOA Albedo Typical of Land Scenes

	PW		O₃		τ_{aod}		ln(Vis/NIR)		P_{sfc}		ω_{aod}		α_{TOA}	
Base State	1 cm		350 dbu		0.15		0		950 mb		0.025		0.2	
ΔInput	0.5	3.0	300	400	0.05	0.35	−1	1	1000	900	0.01	0.05	0.195	0.205
Surface α_{clr}	0.170	0.193	0.175	0.179	0.194	0.147	0.180	0.175	0.174	0.180	0.177	0.177	0.170	0.185
Range α_{clr}	0.023		0.004		−0.047		−0.005		0.006		−0.000		0.015	

[a]Base state atmosphere along with cos(SZA) = 0.5 gives surface albedo α_{clr} = 0.177.

Table 2. Surface Albedo LUT Model Sensitivity to Various Input Variables[a] With Bright Initial TOA Albedo Typical of Snow Scenes

	PW		O_3		τ_{aod}		ln(Vis/NIR)		P_{sfc}		ω_{aod}		α_{TOA}	
Base State	0.8 cm		350 dbu		0.15		0		950 mb		0.025		0.6	
ΔInput	0.1	1.5	300	400	0.05	0.35	-1	1	1000	900	0.01	0.05	0.585	0.615
Surface α_{clr}	0.692	0.782	0.749	0.759	0.756	0.751	0.755	0.753	0.756	0.752	0.752	0.765	0.733	0.775
Range α_{clr}	0.091		0.010		-0.005		-0.002		-0.004		0.013		0.042	

[a]Base state atmosphere along with cos(SZA) = 0.5 gives surface albedo α_{clr} = 0.754.

defined in any footprint. Two arrays define the scene and percentage of each scene within the footprint. We use the first array to act as a pointer to each scene's associated albedo spectral shape and the second array supplies weights for averaging the albedo spectral shapes within the footprint. These two arrays then supply a first estimate of an albedo spectral shape, $\alpha_{fp}(\nu)$ shown in equation (2) where ν represents the 15 spectral intervals of the LFL05 SW radiation transfer code (see Figure 1) and w_i are normalized weights based on the percentage of each IGBP scene type found in any CERES footprint. Integrating this albedo spectral shape gives a broadband albedo A_{fp} flag. Note the IGBP based albedo spectral shapes do not vary over time, except for snow and ice, and so variability in the CERES IGBP vector, and subsequently our albedo spectral shape, is based purely on geography.

$$\alpha_{fp}(\nu) = \sum_{i=1}^{n-scenes} \alpha_i(\nu)w_i \qquad (2)$$

[18] We now have estimates for the CERES footprint of observed surface broadband albedo from the LUT, α_{clr}, and albedo spectral shape from the IGBP map $\alpha_{fp}(\nu)$; the next step is to reconcile the two. This is done simply by multiplying the ratio of α_{clr} to A_{fp} times the albedo spectral shape $\alpha_{fp}(\nu)$ as shown in equation (3).

$$\alpha_{init}(\nu) = \alpha_{fp}(\nu) * \left(\frac{\alpha_{clr}}{A_{fp}}\right) \qquad (3)$$

[19] α_{init} is then the initial spectral albedo input as the surface boundary condition for running LFL05 in CERES/SARB processing for clear sky footprints. The retrieved broadband surface albedo is the ratio of the upwelling and down-welling fluxes at the surface, as computed by LFL05.

[20] Initial broadband surface albedo for footprints viewing land surfaces where CERES has identified clouds is specified in a different manner. Derivation of an albedo spectral shape is identical to that for clear sky. However there is no instantaneous retrieval of a broadband cloudy sky land surface albedo. Instead, a "history" map of albedo is created by preprocessing 1 month of CERES data at a time. Using the LUT in equation (1) all clear sky footprints for a month are examined in advance and the minimum clear sky albedos are saved on a 1/6° equal angle resolution grid. If a grid box is cloudy for the entire month a historical value is retained or the clear sky albedo is based solely on assumed surface vegetation type. To utilize these history map values for cloudy sky footprints we require a method to "move" the broadband albedo from the solar zenith angle at which they were observed to the "diffuse" solar zenith angle (53° the Gaussian quadrature point at which the two-stream is solved) which is used for all cloudy sky calcu-

lations in SARB processing. To accomplish this we chose the diurnal model described by *Briegleb et al.* [1986] shown in equation (4). It assumes a semi-infinite canopy with randomly angled leaves for each vegetation type. Each scene type is assigned a "D" value which defines the amount by which albedo will change as a function of changing solar zenith angle. D values are determined from the same source as the spectral albedo for each IGBP scene type.

$$a(\mu_1) = a(\mu_0)\frac{(1 + D)}{(1 + 2D\mu_1)} \qquad (4)$$

[21] We do not attempt to validate cloudy sky albedos in this paper. Though the limitations of this model have been elucidated [see *Wang et al.*, 2007], due to restrictions on altering CERES climate data products, methodology once established is not changed unless new data product "Editions" are released.

4. Impacts of Aerosols and Albedo Spectral Shape on TOA SW Aerosol Forcing

[22] How important is the assumption for albedo spectral shape of surface reflection when retrieving broadband surface albedo with observations of broadband TOA flux such as CERES? In contrast to the MODIS technique, which uses satellite spectral radiances and a model to explicitly determine spectral reflection at the surface and then follows with an expression for broadband surface albedo, the CERES method is simple. Calculations in this section show that for typical land surfaces, the retrieval of

Table 3. IGBP Scene Types and Source of Albedo Spectral Shape

| Scene Type	Spectral Curve Source
1. Evergreen Needleleaf Forest	*Briegleb et al.* [1986]
2. Evergreen Broadleaf Forest	*Briegleb et al.* [1986]
3. Deciduous Needleleaf Forest	*Briegleb et al.* [1986]
4. Deciduous Broadleaf Forest	*Briegleb et al.* [1986]
5. Mixed Deciduous Forest	*Briegleb et al.* [1986]
6. Closed Shrubland	*Briegleb et al.* [1986]
7. Open Shrubland	*Pinker and Karnieli* [1995]
8. Woody Savanna	*Briegleb et al.* [1986]
9. Savanna	*Zhou et al.* [2001]
10. Grassland	*Zhou et al.* [2001]
11. Permanent Wetland	*Briegleb and Ramanathan* [1982]
12. Cropland	*Zhou et al.* [2001]
13. Urban	*Briegleb et al.* [1986] (18)
14. Crop/Natural Vegetation Mosaic	*Zhou et al.* [2001]
15. Permanent Snow/Ice	*Jin et al.* [1994]
16. Barren/Desert	*Pinker and Karnieli* [1995]
17. Water Bodies	*Jin et al.* [2004]
18. Tundra	*Briegleb et al.* [1986]
19. Fresh Snow	*Jin et al.* [1994]
20. Sea Ice	*Jin et al.* [1994]
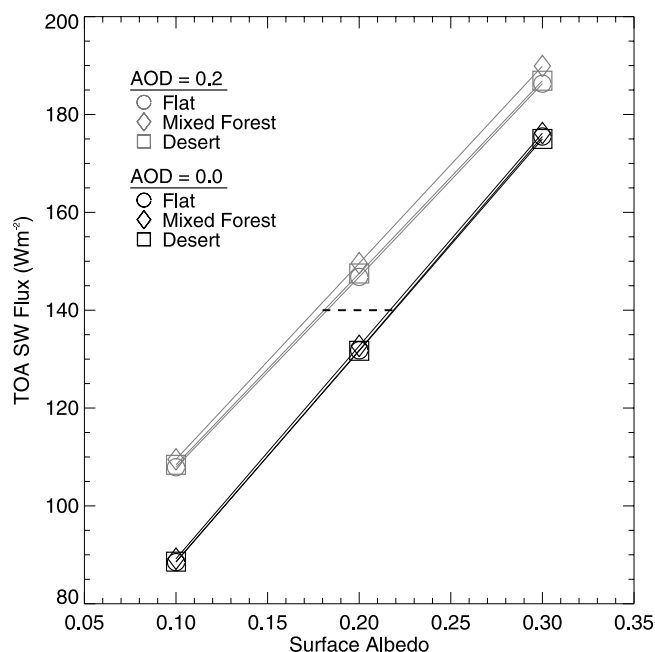
Figure 2. Change in TOA SW flux with change in spectral surface albedo and aerosol optical depth.

broadband surface albedo with broadband TOA albedo as an input parameter is fairly insensitive to the assumed albedo spectral shape of surface reflection; this provides some confidence in the CERES method. It will also be apparent that CERES and MODIS products for surface albedo hinge on the fidelity of their assumptions for aerosols, both of which rely on the MODIS aerosol retrievals of *Remer et al.* [2005]. Also while factors like broadband aerosol forcing at TOA are strongly influenced by the broadband surface albedo [i.e., *Betts et al.*, 2007], the spectral shape of surface albedo can also have a secondary, but significant impact on broadband aerosol forcing.

[23] To analyze this effect we chose three distinct spectral shapes, one for a flat spectral albedo, one for a Mixed Forest scene and one for a Barren Desert scene. The Mixed Forest and Desert shapes are shown in Figure 1. LFL05 calculations with these shapes yield a broadband surface albedo of 0.3 for a midlatitude summer atmosphere and $\mu = 0.5$. Upwelling SW fluxes at TOA from LFL05 are shown in Figure 2. These runs are based on three spectral shapes (Mixed Forest, Barren Desert, and spectrally flat), different values for integrated broadband surface albedo (0.1, 0.2, 0.3) and aerosol optical depths (0.0, 0.2) of OPAC continental aerosol. At the TOA we find the first order effect is, of course, the increase in broadband surface albedo. The lower triplet of lines for aerosol free conditions are nearly coincident; here a retrieval of broadband surface albedo with an observed broadband flux at TOA is almost insensitive to the assumption for spectral shape. The second order effect is the change in AOD, which, regardless of spectral shape for surface reflection, increases the TOA SW flux very linearly with broadband surface albedo. The dashed line in Figure 2 shows that for a given value of observed SW at TOA, an error of 0.2 in the specification of AOD

would yield an error of 0.04 in the retrieved broadband surface albedo.

[24] The effect of albedo spectral shape is small but not negligible, and is larger when aerosol is included in the calculation. In general, if one fixes albedo spectral shape and decreases broadband surface albedo, the effect will be to increase the aerosol forcing to TOA SW flux. This is shown in Table 4 where we have used our predetermined spectral shape for Mixed Forest. At a solar zenith angle of 60°, a change in broadband albedo from 0.3 to 0.2 results in a change in aerosol forcing at TOA of over 3 W m^{-2}. Hence a 33% reduction in broadband surface albedo (0.3 to 0.2) is compensated by an approximately 28% increase in TOA aerosol forcing to SW flux (11.9 W m^{-2} to 15.2 W m^{-2}).

[25] In Table 5, one finds that changing albedo spectral shape but keeping broadband albedo fixed, results in a change in aerosol forcing to TOA SW that is smaller, 1.4 W m^{-2}. Although this is only half the change to aerosol forcing of that effected by the broadband albedo change of 0.1 (0.2 versus 0.3) in Table 4, it remains notable.

[26] A final way to consider the effect of albedo spectral shape on TOA aerosol forcing is to look at the spectral forcing at the TOA as a function of aerosol type. Figure 3 does this by showing the aerosol forcing to TOA albedo spectrally for two different aerosol types with fixed aerosol optical depth of 0.2. Again the mixed forest spectral shape (small reflection in the visible but sharply larger in the near infrared) is used in the radiation transfer calculation and spectral forcing in the LFL05 bands is shown for a continental aerosol (solid circles) and 2 μm dust particles (open circles). Though total broadband aerosol forcing is approximately the same, spectrally the effect is quite different for the two aerosol types. The continental aerosol particles are small and have most of their impact in shorter wavelengths.

5. Assessment of CRS Surface Albedo

[27] *Jin et al.* [2003] and others have pointed out that validation and assessment of satellite based surface albedos is in essence a scaling problem. In their paper validating MODIS BRDF based surface albedo they compared their results against a number of various sources including observations from 10-m towers at several locations around the United States and scaling up 30 m LANDSAT data to the 1 km MODIS pixels. They used a minute-by-minute time series of observed downwelling SW at the surface [*Long and Ackerman*, 2000] to exclude surface albedos measurements made under cloudy conditions from their comparison. MODIS gives distinct surface albedo products for "white sky" (isotropic illumination) and "black sky" (clear sky) conditions. By weighting MODIS black/white sky albedos by observed direct/diffuse incoming SW flux at the surface, *Jin et al.* [2003] were able to match 10-m tower albedo observations to within an absolute accuracy of ~0.02 albedo units for most months of the year.

Table 4. Effect of Decreasing Broadband Surface Albedo on Aerosol Forcing to SW Flux up at TOA

α_{sfc}	SW up TOA (Clear Sky, AOD = 0.2)	SW up TOA (Pristine, AOD = 0.0)	Aerosol Forcing (Clear − Pristine)
0.3	189.4 W m^{-2}	177.5 W m^{-2}	11.9 W m^{-2}
0.2	148.8 W m^{-2}	133.7 W m^{-2}	15.2 W m^{-2}

Table 5. Effect of Differing Spectral Albedo Shape on Aerosol Forcing to SW Flux up at TOA

Spectral Shape	SW up TOA (Clear Sky, AOD = 0.2)	SW up TOA (Pristine, AOD = 0.0)	Aerosol Forcing (Clear − Pristine)
Mixed forest	189.4 W m^{-2}	177.5 W m^{-2}	11.9 W m^{-2}
Desert	187.6 W m^{-2}	177.1 W m^{-2}	10.5 W m^{-2}

5.1. Comparison of CRS Albedo to Ground Observations

[28] For the assessment of our derived clear sky albedos we have selected a number of regions where CERES data is routinely subset for validation purposes. Chosen are 25 locations scattered about the globe based on both their scene type and availability of surface observed albedo. All comparison locations are shown in Figure 8. The sites that include ground observations of albedo include the Department of Energy's Atmospheric Radiation Program (ARM) Southern Great Plains sites, NOAA's Global Monitoring Division (GMD) Surface Radiation (SURFRAD [*Augustine et al.*, 2000]) and several Baseline Surface Radiation Network (BSRN) project [*Ohmura et al.*, 1998], all of which adhere to the strict observational standards set by the BSRN project guidelines.

[29] The assessment of CRS surface albedo with ground measurements is even more problematic than the MODIS albedos because of the enormous footprint size (Figure 4). Most surface observation sites are fenced, often a 10-m tower viewing only a patch of grass that is surrounded by a different ecosystem (i.e., land grazed by cattle or used to grow crops). This incompatibility was seen by *Roesch et al.* [2004] when they compared MODIS to surface observations. This is confirmed in Figure 5 where CRS data and the MODIS 5 km pixel closest to a surface site are compared to a number of surface observed albedos from 14 locations within our set of validation sites where albedo is observed at the surface. Because most of the spatial inhomogeneities that influence surface reflection over land are generally constant, it is then not possible to "trade space and time" as was successfully done for ocean albedo [*Jin et al.*, 2005] during the CLAMS campaign [*Smith et al.*, 2005]. In contrast to the MODIS validation of *Jin et al.* [2003], the surface albedos of CRS and MODIS (described in the next section) in Figure 5 are investigated at the footprint scale of CERES; ground measurements of the downwelling direct/diffuse ratio are not used to adjust the satellite-retrieved albedo; and ground measurements are not used to screen for cloud effects.

[30] For all 4 months considered CERES and MODIS derived albedos are on average lower than observations from, on average, −0.02 up to −0.05% absolute. This translates into 10% to 25% differences in albedo relative to the surface observations. The comparison might be more favorable if the view from 10 m approximated the surrounding landscape on a much larger scale. However snow cover, which is often extensive, can produce sharp seasonal contrasts in surface albedo over large areas that are faithfully represented by point measurements. Figure 6 shows a time series over five years comparing observed albedo and CRS surface albedo at the SURFRAD Fort Peck, MT site [*Augustine et al.*, 2000]. For this plot, points represent the mean albedo for a month, retrieved or observed, where that monthly mean is calculated solely at the time of the CERES observation. The Terra overpass is typically at about 1030 LST, so these are not true diurnal monthly mean values. In Figure 6 we find the SARB algorithm described in the preceding sections accurately captures interannual variability in albedo particularly due to snow events.

5.2. MODIS Surface Albedo (MCD43C2)

[31] Our comparisons to this point have not been consistent in scale (Figure 4): The surface albedos in Figures 5 and 6 are measured (retrieved by CRS) at scale of 10 m (30 km). The MODIS retrievals described below and seen in Figure 5 are at a 5-km scale. In this section we scale MODIS products up to the larger size of the CERES footprints (Figure 7). Such a consistent footprint-to-footprint approach is recommended by the Committee on Earth Observation Satellites (CEOS) Working Group on Calibration/Validation (WGCV), Land Product Validation (LPV) albedo subgroup (http://lpvs.gsfc.nasa.gov/). We have chosen the MODIS data product MCD43C2 v005 to compare with surface albedo produced from the upward/downward ratio of CRS flux calculation under clear skies. MCD43C2 is a snow free
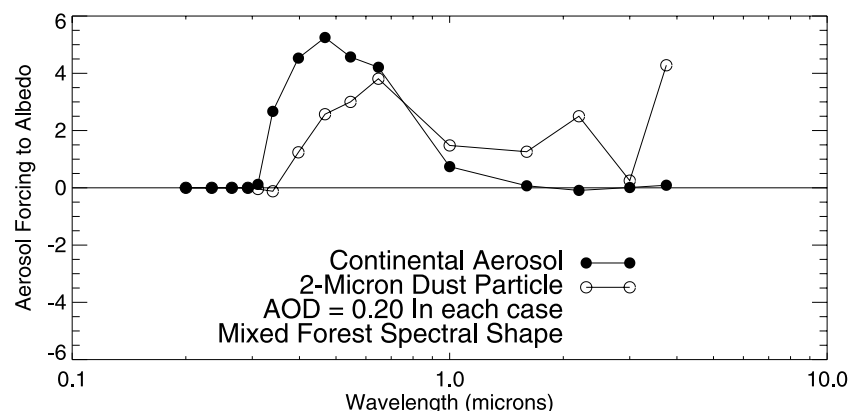
Figure 3. Spectral forcing of TOA albedo due to two different aerosol types.
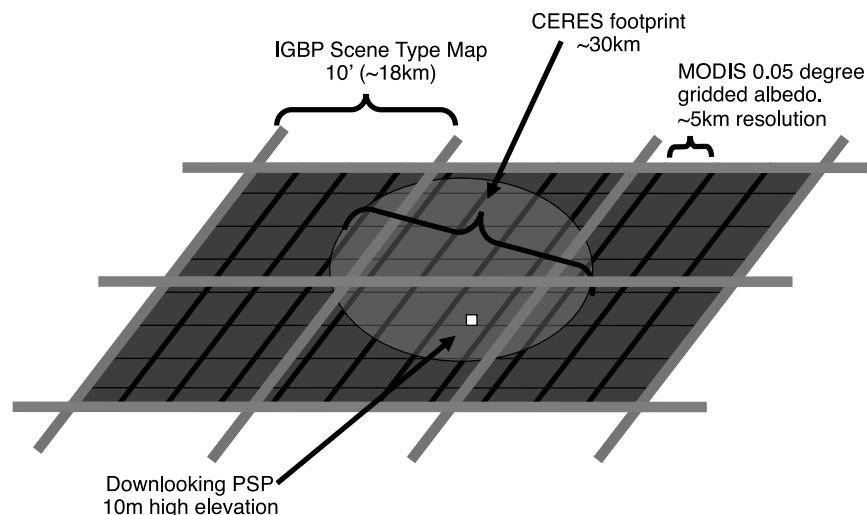
Figure 4. Cartoon showing CERES footprint, MODIS grid, and IGBP grid relative to one another.

gridded data product with 0.05° equal angle spatial resolution. The gridded product is described in detail by *Gao et al.* [2005]. This resolution corresponds to an approximate 5 km "pixel" size. Temporally, the MODIS Version 5 algorithm delivers empirical BRDFs from clear sky MODIS imager data every eight days using overlapping 16-day windows [*Lucht et al.*, 2000b; *Schaaf et al.*, 2002]. The MODIS BRDF/Albedo algorithm is similar to other kernel-driven schemes used to obtain anisotropy and albedo information

used by the POLarization and Directionality of the Earth's Reflectances (POLDER) instrument [*Hautecœur and Leroy*, 1998; *Bicheron and Leroy*, 2000; *Maignan et al.*, 2004; *Bacour and Bréon*, 2005] satellite sensor and Meteosat Second Generation (MSG) SEVIRI instrument [*van Leeuwen and Roujean*, 2002; *Geiger et al.*, 2004]. Coefficients modeling the isotropic, volume, and geometric-optical surface scattering of observed vegetation and surface elements are derived for direct ("Black Sky") and wholly diffuse
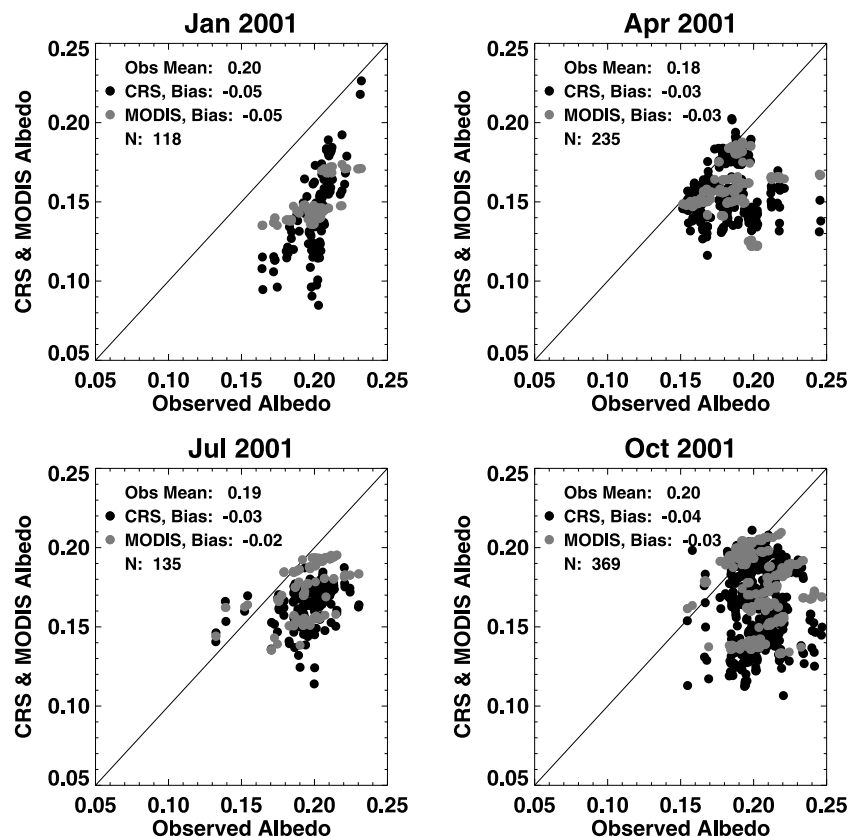

Figure 5. CERES CRS and MODIS 5 km albedo compared to observed surface albedos at 14 land surface sites during 4 months in 2001.
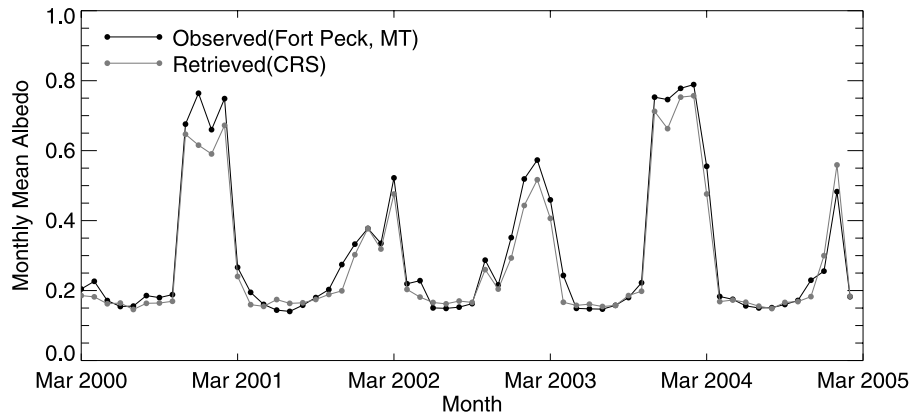
Figure 6. Time series of observed (black) and CRS retrieved albedo near Fort Peck, MT. Values represent a mean for the month at the time of CERES observations.

("White Sky") radiation. These coefficients represent the 16-day window. They are recombined to form albedo (both spectral and broadband) using equation (5).

$$\alpha(\nu) = \alpha_{ws}(\nu) * C(\mu, \tau_{aod}, T_{aod}) + \alpha_{bs}(\nu)$$
$$* (1 - C(\mu, \tau_{aod}, T_{aod})) \qquad (5)$$

[32] The total albedo, at the seven spectral intervals and three broadbands indicated as ν is then a linear combination of the white (α_{ws}) and black (α_{bs}) sky albedos (which are derived directly from the coefficients supplied on the MCD43C2 data product) and the coefficient C which is given by a look-up table that is a function of aerosol optical depth, aerosol type Continental (chosen for all calculations in this comparison) or Maritime, MODIS wavelength, and solar zenith angle. The look-up table is supplied along with the data product. Spectrally, the product supplies seven narrowband visible and near infrared channels and three broadband estimates based on weighting functions described by *Liang et al.* [1999]. These data have been validated in several publications. The accuracy of the MODIS operational albedos marked as high quality by the quality assurance flags is less than 5% relative at validation sites studied thus far and even those albedo values with low quality flags have been found to be within 10% relative of field data [*Jin et al.*, 2003; *Salomon et al.*, 2006]. To match the CERES footprints temporally with MODIS data we have restricted the CERES observations to within the 16-day period of the MCD43C2 data product and selected only two MODIS files per month. For example, in January 2001 we chose MODIS files dated January 1 and January 17. The BRDFs in these files are drawn from clear sky MODIS pixels from January 1 through January 16 and January 17 through February 1 respectively, the same time periods within which we match the CERES footprints to the MODIS data. This avoids the possibility of selecting a CERES footprint for more than one comparison. The MODIS Collection 4 AOD (the actual MOD08 retrieval is preferred but the interpolated daily average MOD04 or MATCH aerosol assimilation are more commonly used) is an important parameter in the determination of the CRS surface albedo by CERES. In contrast, the MCD43C2 v005 coefficients for a 16-day window employed MODIS Collection 5. To achieve a footprint-by-footprint comparison

(i.e., recommendation of CEOS) that is more relevant to users (note last paragraph of Introduction), we express the MODIS surface albedo from the MCD43C2 v005 coefficients with the same Collection 4 AODs used by CRS.

5.3. Integration of MODIS Into a CERES CRS Footprint Field of View

[33] Matching the MODIS data to the CERES field-of-view is necessary for an appropriate comparison of the two
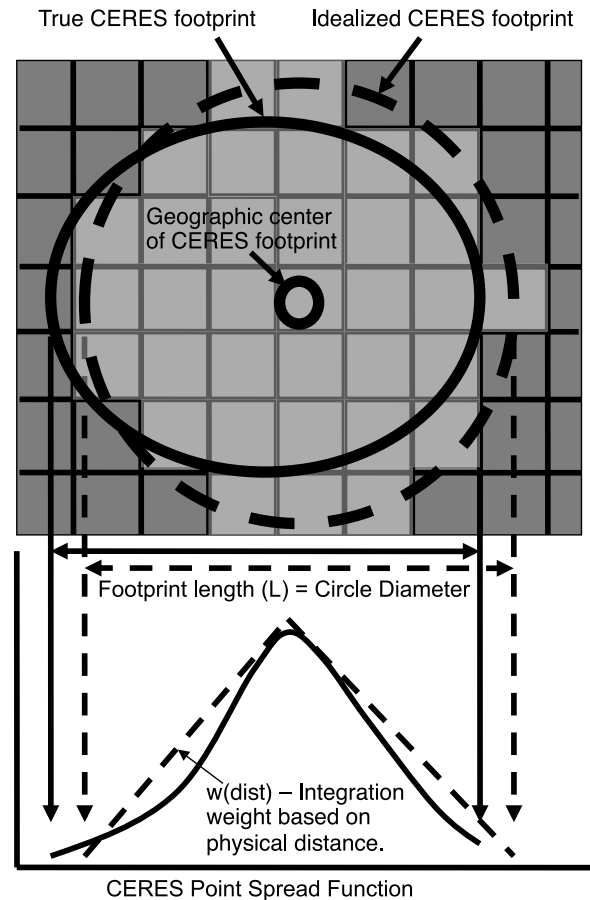

Figure 7. Schematic of placement of MODIS gridded "pixels" inside of larger CERES footprint and integration weights.
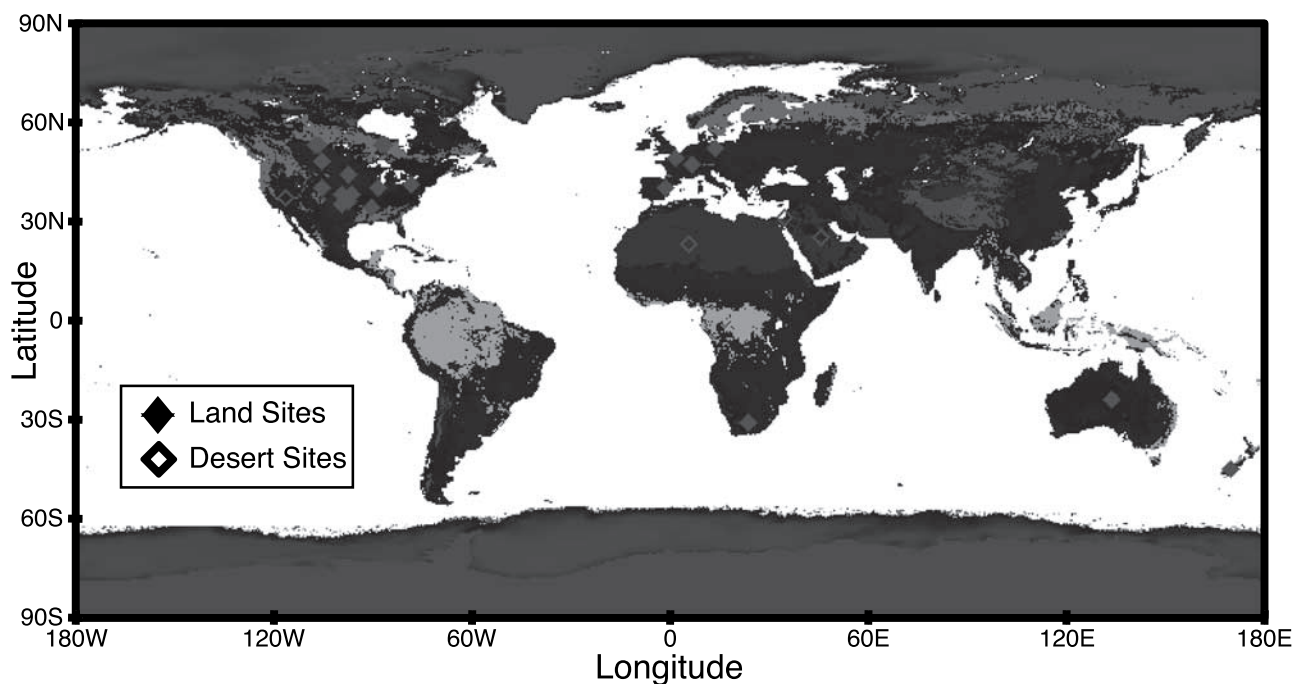
Figure 8. Map showing locations on the globe where the CERES and MODIS albedos are collocated for comparison. Sites are divided into 25 land and 4 desert locations.
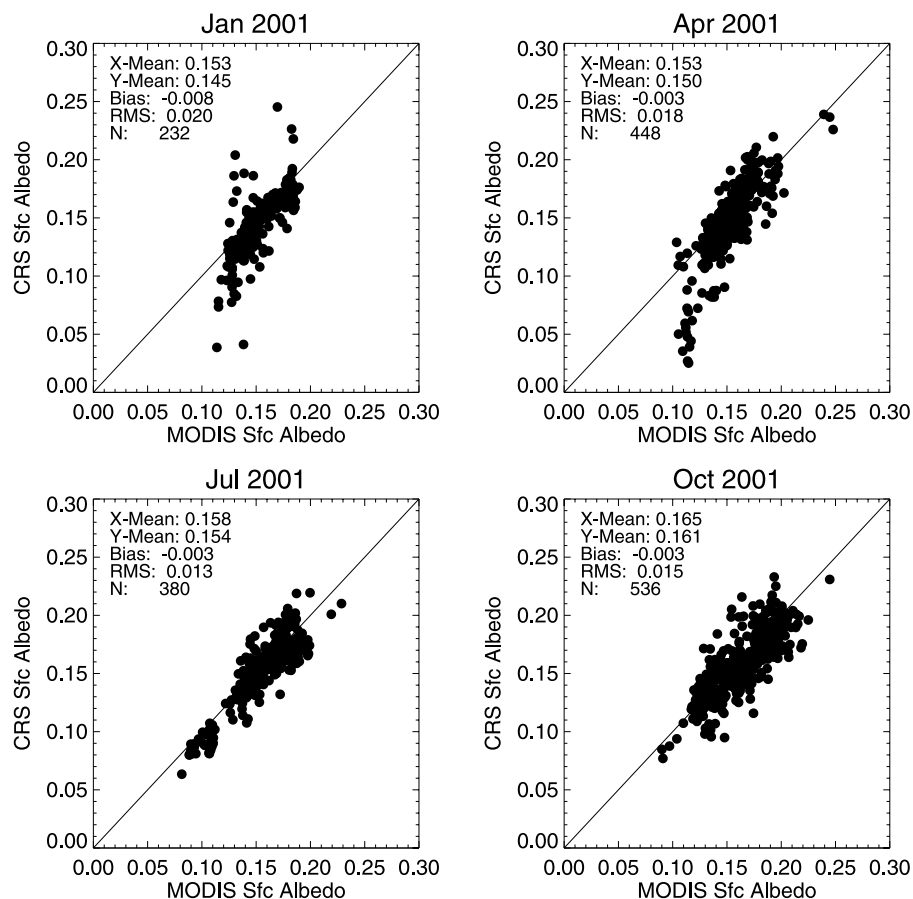

Figure 9. Comparison of CRS surface albedo to MODIS albedo integrated within coincident CERES footprints.

Table 6. Monthly Mean Albedo Differences Between CRS Albedo and MODIS Albedo Integrated Within CERES Terra FM1 for Land Footprints for 4 Months in 2001

	January	April	July	October	All Months
CRS mean	0.145	0.150	0.154	0.161	0.154
MODIS mean	0.153	0.153	0.158	0.165	0.158
Absolute bias	−0.008	−0.003	−0.003	−0.003	−0.004
Absolute RMS	0.020	0.018	0.013	0.015	
Relative bias	−5.2%	−2.0%	−2.0%	−1.8%	−2.4%

products. The term "footprint" refers to a CERES field-of-view (FOV) of the surface while the term "pixel" will be defined as the MCD43C2 0.05° grid box. Our methodology for matching MODIS pixels to the CERES footprint follows this path. We locate a CERES footprint center on the 0.05° MODIS grid and determine footprint length. The footprint itself is associated with a smoothly varying "point spread function" (PSF) that describes the change in detector response with respect to the location of an energy source within the footprint. This energy response changes as a function of viewing zenith angle (VZA), elongating in the forward view and compressing in the back as shown schematically in Figure 7. Hence the center of a CERES footprint (given as a latitude and longitude at the surface in all CERES data products) is the energetic center with respect to view zenith angle (Figure 7). The length and shape of a footprint thus changes from a near circle with diameter ~30 km at nadir view angle, to an ellipsoidal shape with length near 200 km at 70°VZA. When integrating other variables within a CERES footprint one needs to take this energy response into account giving less weight to pixels near the edge of the footprint and more weight to pixels near the center.
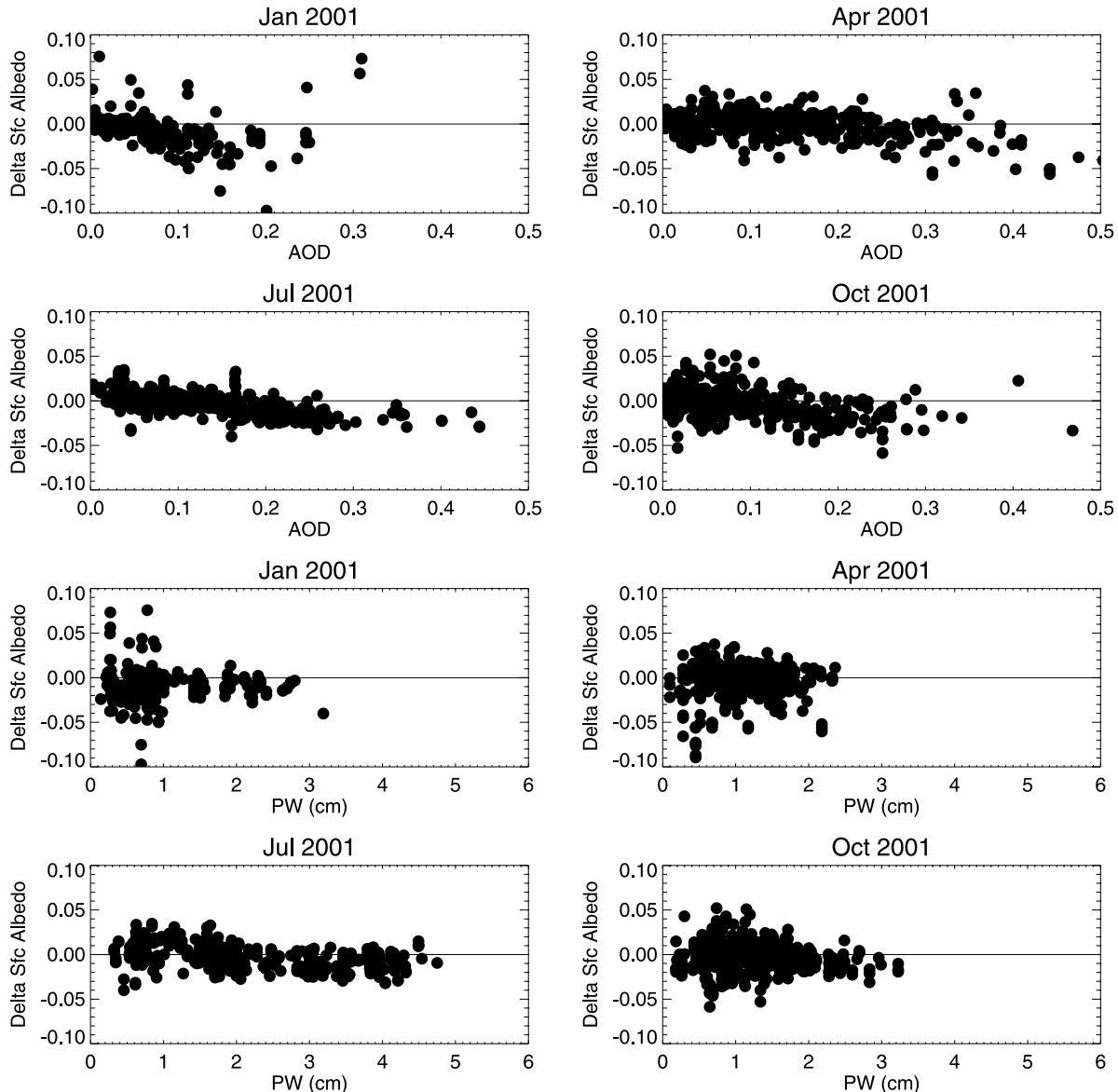

Figure 10. Difference in CRS and MODIS albedo as a function of aerosol optical depth and precipitable water used in CRS calculations.
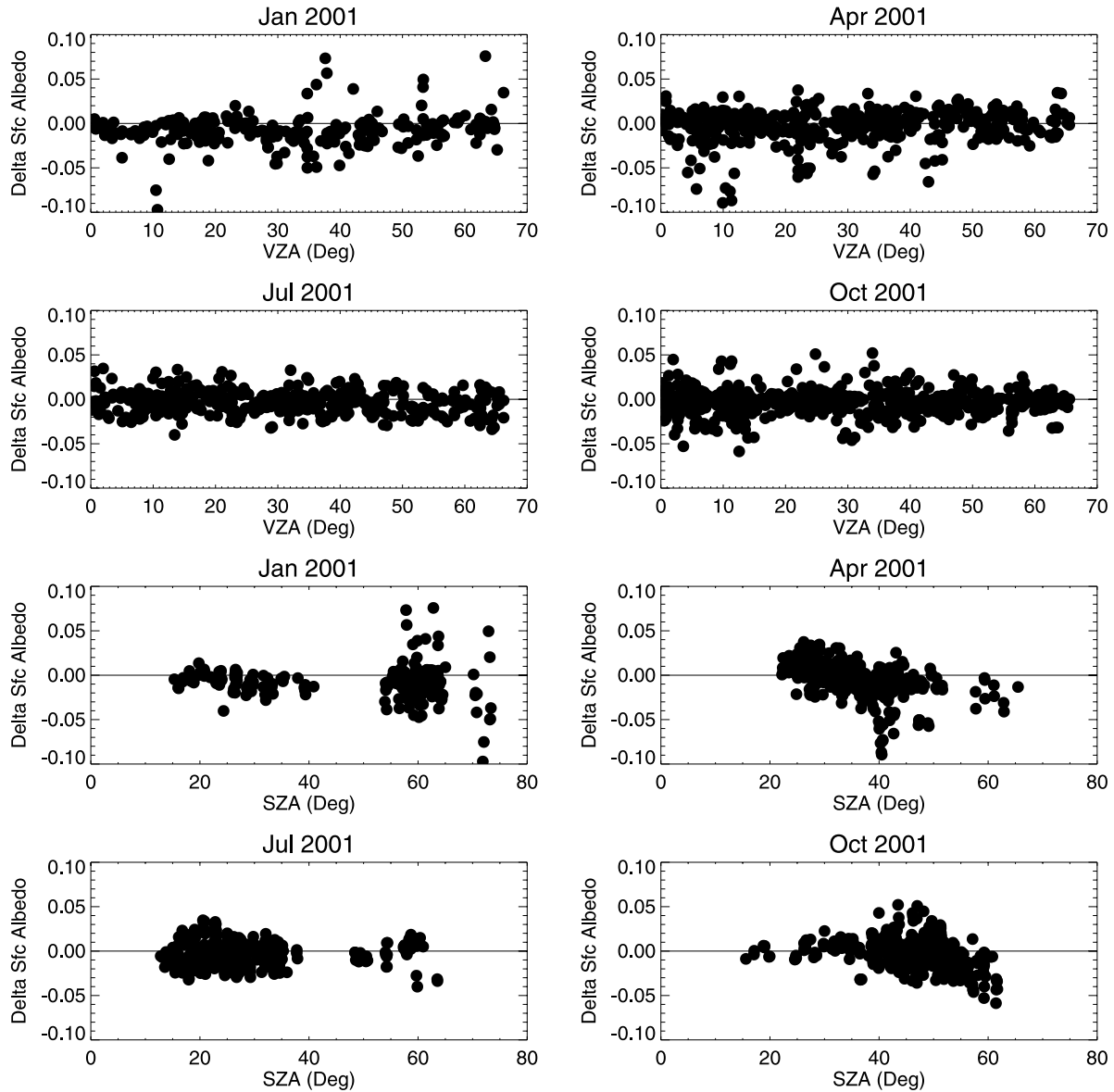
Figure 11. Difference in CRS and MODIS albedo for "land" validation sites as a function of viewing zenith (VZA) and solar zenith (SZA) angle at time of CERES observations.

[34] For the purposes of this study we assume the CERES footprint is a circle whose center is located by the CERES surface latitude/longitude with a radius of 1/2L (where L is the length of the CERES footprint along the scan angle.) We approximate the energy response of the instrument as a normalized distance of 1/L from this center. MODIS albedos are then integrated within the CERES footprint, weighting the MODIS regions as d/L where "d" is the physical distance from the footprint center to the center of the MODIS pixel. At nadir viewing angles the CERES footprint will closely match with our assumption. However as VZA increases the circular shape and actual area viewed will begin to diverge. The more heterogeneous the surface is in elevation, scene type etc.. . . the more error we might expect due to these assumptions.

[35] In this comparison we only consider footprints free of clouds as determined in the CERES data product. CERES CRS product includes an independent cloud analysis of

MODIS 1 km observations within each CERES footprint [*Minnis et al.*, 2003]. We only consider footprints where the CERES cloud fraction is 0.0, which is to say the cloud algorithm determined all collocated MODIS 1 km pixels to be cloud free. At times, the MODIS BRDF albedo upon which we locate the CERES footprint is incomplete. We interpolate the MODIS BRDF coefficients in space if the missing portion of the field is less than 20% of the footprint. Otherwise we disregard that footprint.

6. Results of CRS and MODIS Broadband Albedo Comparison

6.1. Assessment of CRS Broadband Surface Albedo at "Land" Sites

[36] In this section we compile results of the MODIS surface albedo integrated within CERES footprints for eight MCD43C2 data files. Chosen were the months of January,
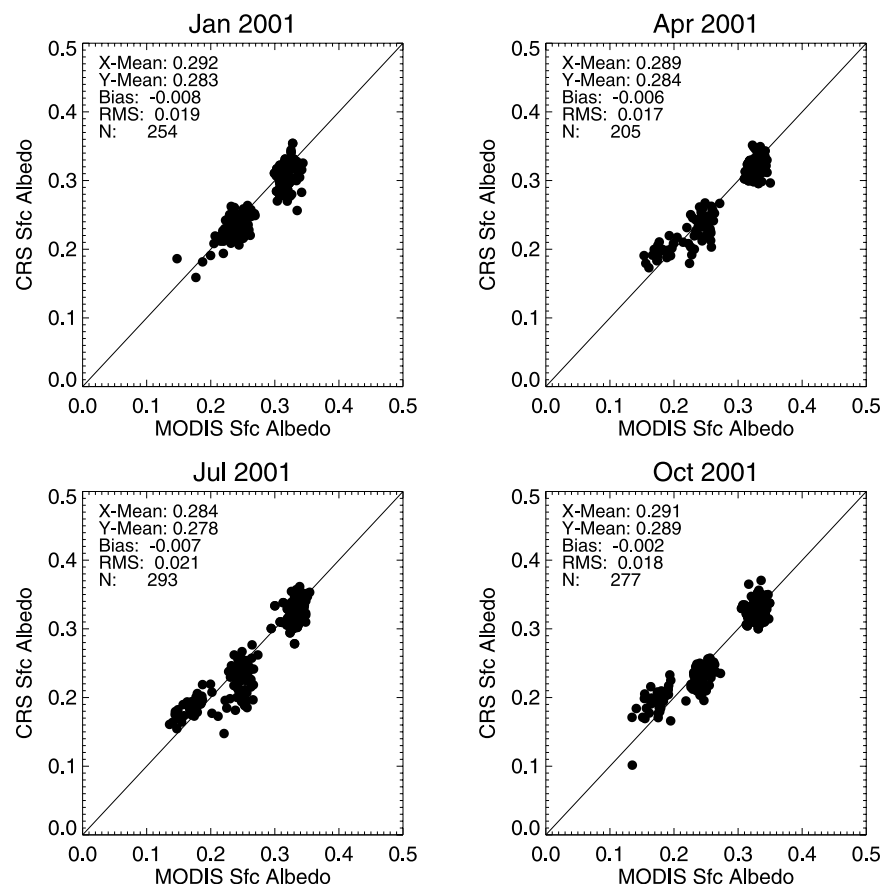
Figure 12. Comparison of CRS and MODIS albedo at four desert locations around the globe.

April, July, and October 2001. Figure 8 shows the locations on the globe where comparisons were made. These regions were previously designated "CERES validation regions" and are approximately 111 km square regions where subsets of CERES data are extracted from formal data processing for the purpose of validating CERES algorithms. For our purposes we retain only footprints whose center is less than 25 km from each surface site for each satellite overpass to limit the sample. Black filled diamonds indicate land surface sites and open diamonds are designated desert surface sites.

[37] Complete results for 25 land sites for the months considered are shown in Figure 9. The majority of these sites are located in the northern hemisphere. Subsequently the number of clear sky comparisons peak in October whereas in January, due to snow in the scenes, which has been removed, we find the least number of clear sky comparisons. Though there is some seasonal variability, overall the comparisons are quite good as measured by mean bias and RMS for each month as shown in Table 6. Bias for all months is negative with a mean of −0.004 absolute, leaving a relative bias of just −2.4% (as if CERES were "darker" than MODIS). The RMS runs from a low of 0.013 in July to 0.020 in January.

[38] The conspicuous "tail" of low CRS albedos in April 2001 (Figure 9b) is largely due to data from a single location (north latitude 53.5, longitude 273.9) with evergreen forest to the south of Hudson Bay in eastern Canada (Figure 8). There, MODIS albedo remains stable near 0.10

while the CRS albedo varies between 0.03 and 0.13. The reasons behind the retrieved surface albedos (as low as 0.03), which is so low as to strain credibility for a large footprint over land, is instructive for the EOS user. Collection 4 AOD reported by the MODIS Atmosphere Team for this site in April 2001 are both quite high and quite variable. The algorithm used by the MODIS Land Team preferentially chooses cloud-free pixels with low AOD (less obscuration) for the retrieval of surface albedo, so MCD43C2 v005 coefficients supplied by the MODIS Land Team are generally founded on the low AOD observations in each 16-day block. While equation (5) shows that the MODIS surface albedo explicitly depends on AOD, the day-to-day change in AOD has only a fairly small effect by apportioning the fraction of "white" and "black" sky. The dashed line in Figure 2 draws attention to the contrasting large impact of any change in AOD on the CRS albedo. As

Table 7. Monthly Mean Albedo Differences Between CRS Albedo and MODIS Albedo Integrated Within CERES Terra Footprints at Four Desert Locations for 4 Months in 2001

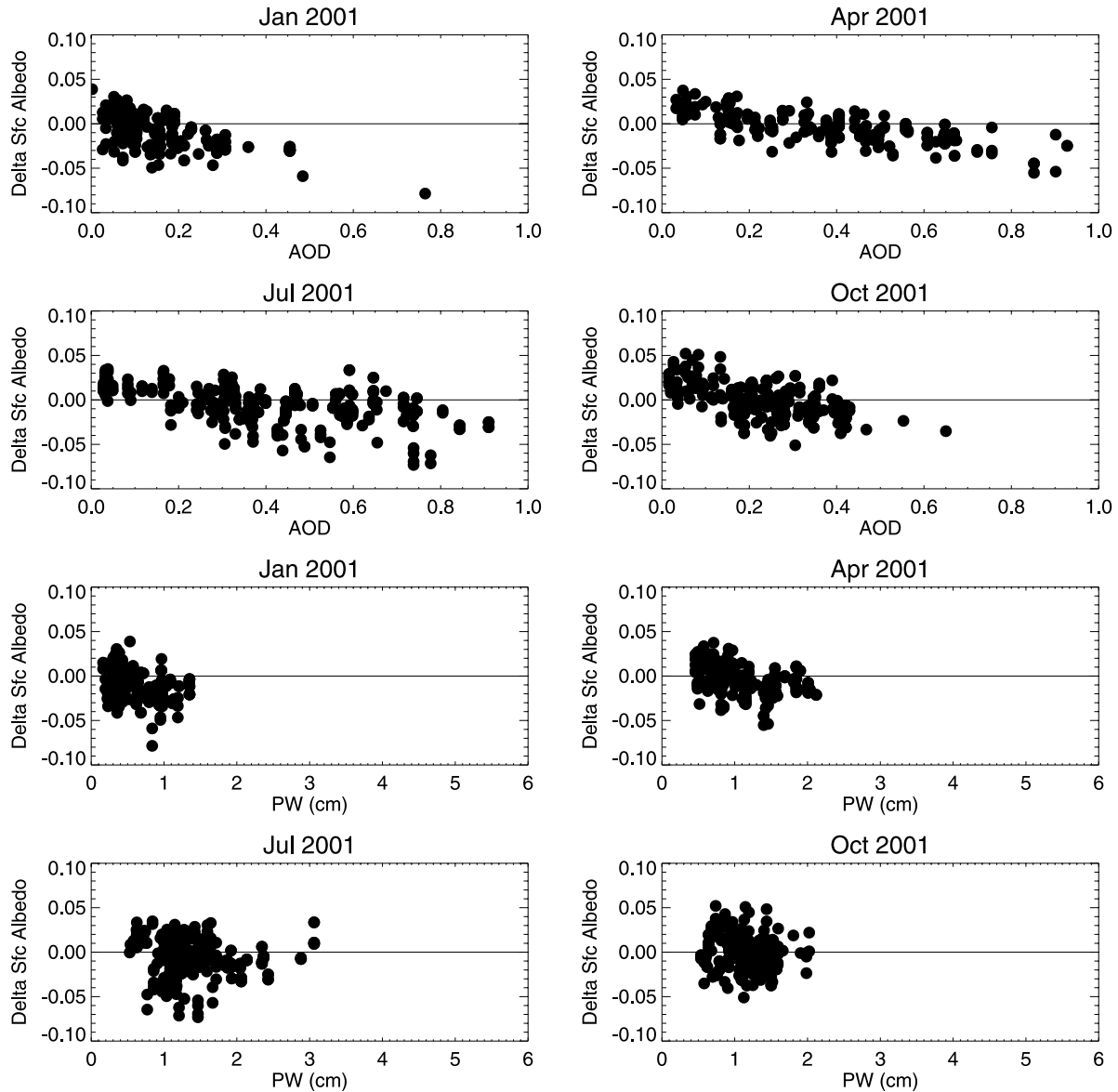|	January	April	July	October	All Months
CRS mean	0.283	0.284	0.278	0.289	0.283
MODIS mean	0.292	0.289	0.284	0.291	0.289
Absolute bias	−0.008	−0.006	−0.007	−0.002	−0.006
Absolute RMS	0.019	0.017	0.021	0.018	
Relative bias	−2.7%	−2.1%	−2.5%	0.7%	−2.1%

Figure 13. Difference between CRS and MODIS albedo at desert locations as a function of aerosol optical depth and precipitable water.

MODIS pixels are very small, there are usually a sufficient number in a local domain for the 16-day reporting period for the MODIS surface albedo product. Because CERES footprints are large, they are often not clear. Thus every available clear CERES footprint over land is used to retrieve a surface albedo, regardless of AOD. For the site in eastern Canada in April 2001, CRS reported 20 clear footprints with simultaneous retrievals of AOD by MODIS. The thirteen CERES CRS footprints with high AOD (mean 0.67) gave an unrealistically low mean surface albedo of 0.05; the other seven (mean AOD of 0.32) had a mean albedo of 0.11. The surface albedos from the MODIS Land Team are in this case (the tail) more realistic than those from CERES, and the source of this CERES deficiency in surface albedo appears to lie in some surprisingly high values of AOD from the MODIS aerosol product. The range of expected values from the MODIS v004 aerosol product defined by *Remer et al.*

[2005] is $\pm 0.05 \pm 0.15\tau_{aod}$ when compared to surface observed aerosol from the AERONET network. Though high, it is unknown if the value of .67 lies outside this range as there is no surface observation against which to compare. However the LUT sensitivity is largest to aerosol optical depth over snow free land albedos as shown in Table 2. If the radiative transfer calculations with the MODIS surface albedos were run for the high AOD cases, they would yield TOA albedos much larger than those observed with the CERES broadband instrument; we know this because the CRS calculations (having low surface albedos) agree with CERES observations. Such a conspicuous tail of low albedo (Figure 9b) is not found to the same degree in any other month. However the CRS routine of retrieving a surface albedo value for every clear CERES footprint over land, regardless of the uncertainty for the input AOD, has yielded
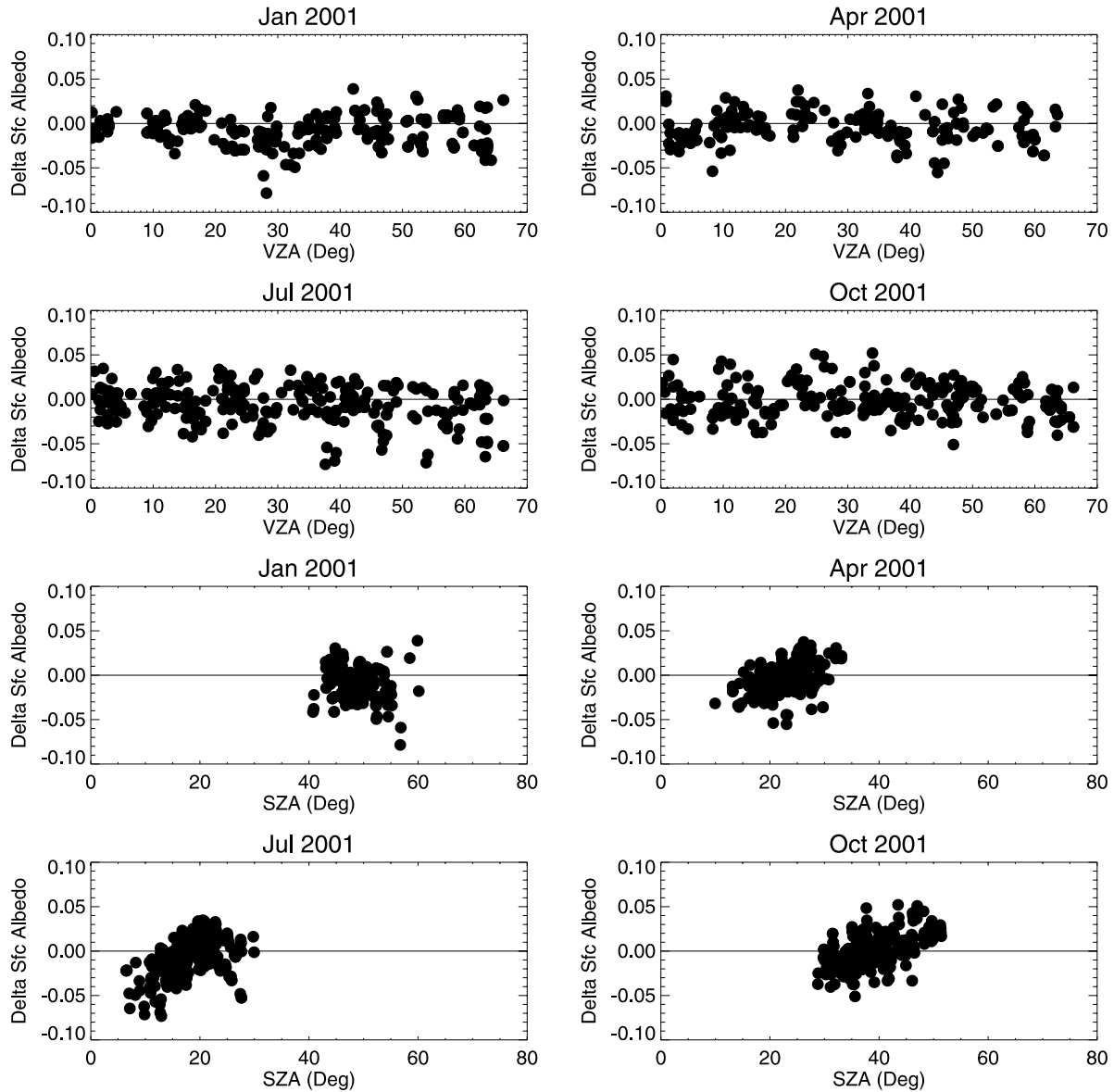
Figure 14. Difference in CRS and MODIS albedo for "desert" validation sites as a function of viewing zenith (VZA) and solar zenith (SZA) angle at time of CERES observations.

a product which is much more noisy than MODIS; note the results for 14 sites in Figure 5.

[39] Departing the tail of Figure 9b, we return to the domain of 25 sites for all 4 months. In Figures 10 and 11 we show the difference between CRS and MODIS albedos as a function of AOD and precipitable water (Figure 10) and solar zenith and viewing zenith angles (Figure 11). In each case there appears little functional relationship except for the case of aerosol optical depth where differences typically increase as AOD increases. Recall that while MODIS albedos (equation (5)) assume only two aerosol types (continental or marine), the MATCH assimilation used by CERES supplies up to seven types (large dust, small dust, sulfate, marine, soot, soluble organic carbon, and insoluble organic carbon) that are used to assign the spectral single scattering albedos and asymmetry parameters. The atmospheric correction used in the CERES retrieval of surface albedo includes the effect of absorption by aerosols that are more variable than in the MODIS retrieval.

6.2. Assessment of CRS Broadband Surface Albedo at "Desert" Sites

[40] Figure 12 and Table 7 compare surface albedos at four desert sites only. Again, this comparison is quite good both visually and in terms of absolute and relative biases, −2.1% for desert versus −2.4% for all sites. Despite the larger mean surface albedo over deserts, the homogeneous nature of the desert scenes produces values for the absolute RMS (Table 7) that are hardly larger than those for all sites (Table 6). The four desert sites (Figure 12 and Table 7) can be placed in three categories: Albedos less than 0.2 come from the SURFRAD Desert Rock, NV (DRA) site. Those between 0.2 and 0.3 are located at the BSRN, Tamanrasset, Algeria (TAM) site. Albedos greater than 0.3 come from the
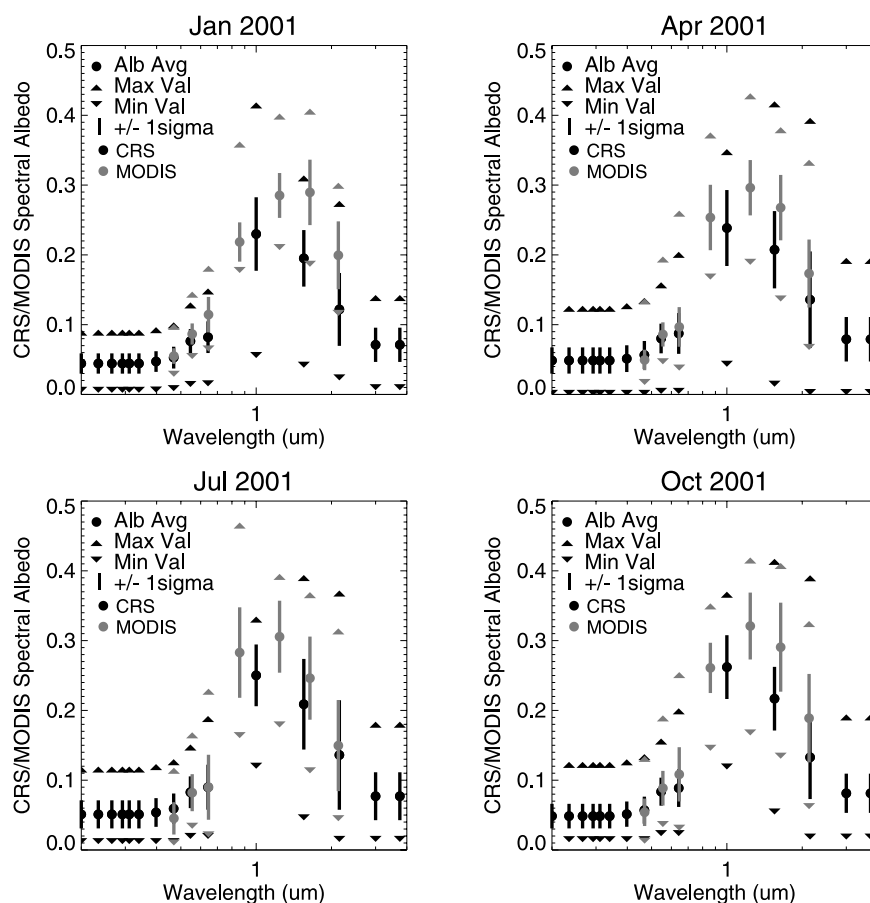
Figure 15. Land surface spectral albedo for CRS in 15 Langley Fu and Liou bands (black) and 7 MODIS channels (gray) shown as a mean (solid circles), maximum and minimum values (up/down triangles), and 1 standard deviation for all comparison points (vertical lines).

BSRN, Sede Boqer, Israel (SBO) site and the Saudi Solar Village (SSV [*Myers et al.*, 1999]) site. Each of the three desert categories displays a characteristic bias: At DRA CRS albedo is consistently greater than the MODIS. At TAM, CRS albedo is consistently lower than MODIS. Also at SBO and SSV the two retrievals tend to agree.

[41] The difference of CERES and MODIS albedos in Figure 13 (the desert analog to Figure 10) again shows little relationship to precipitable water, but a stronger dependence on AOD. For the deserts however there is significantly more aerosol found (note that the *x* axis scale has doubled over that shown for the land sites in Figure 10). Figure 14 shows the difference between MODIS and CRS albedos as a function of VZA and SZA. The "clumping" of footprints as a function of VZA shows that regionally there is dependence of the comparison on view zenith angle, at times approaching 1% to 2% absolute albedo. Likewise with solar zenith angle, in every season but January there appears a positive trend of the difference as SZA increases. When the desert data are broken down site by site, the majority of the solar zenith angle dependence is attributable to footprints at TAM during April, July and October but not January. The effect is exacerbated by the fact that DRA has a permanent positive bias. The reason for the dependence at TAM during Northern Hemisphere summer is at this point unknown though one possibility may be the fidelity of the MODIS BRDF model. At these times at TAM there was very little Collection 5 aerosol available to the land surfaces group for the derivation of the BRDF.

6.3. Assessment of CRS Albedo Spectral Shape

[42] Surface albedo input into LFL05 model is in 15 spectral bands between 0.2 μm and 4.0 μm. As stated above spectral shape used in SARB is solely a function of the (up to eight) spectral shapes based on the IGBP types found in the CERES footprint. CERES/SARB has compiled only 16 different IGBP types, each with a respective spectral shape, to span the globe; the coverage of snow and ice is the only seasonality. On the other hand, MODIS BRDFs and albedos are not constrained to such assumptions for albedo spectral shape, as they are retrieved using MODIS radiances from seven narrowband channels. MODIS albedo spectral shapes themselves are of course dependent on the ability of the MODIS algorithm to retrieve a representative BRDF model given available clear sky radiances retrieved over each 16-day period. Over snow, desert (with heavy aerosol loading) and persistently cloudy areas the MODIS BRDF can and does, revert to a default model which is noted in MCD43C2 quality parameters within the MODIS data product. So whereas we might assume that CERES has the greater potential to retrieve a quality broadband surface albedo, the MODIS instrument is capable of retrieving a better
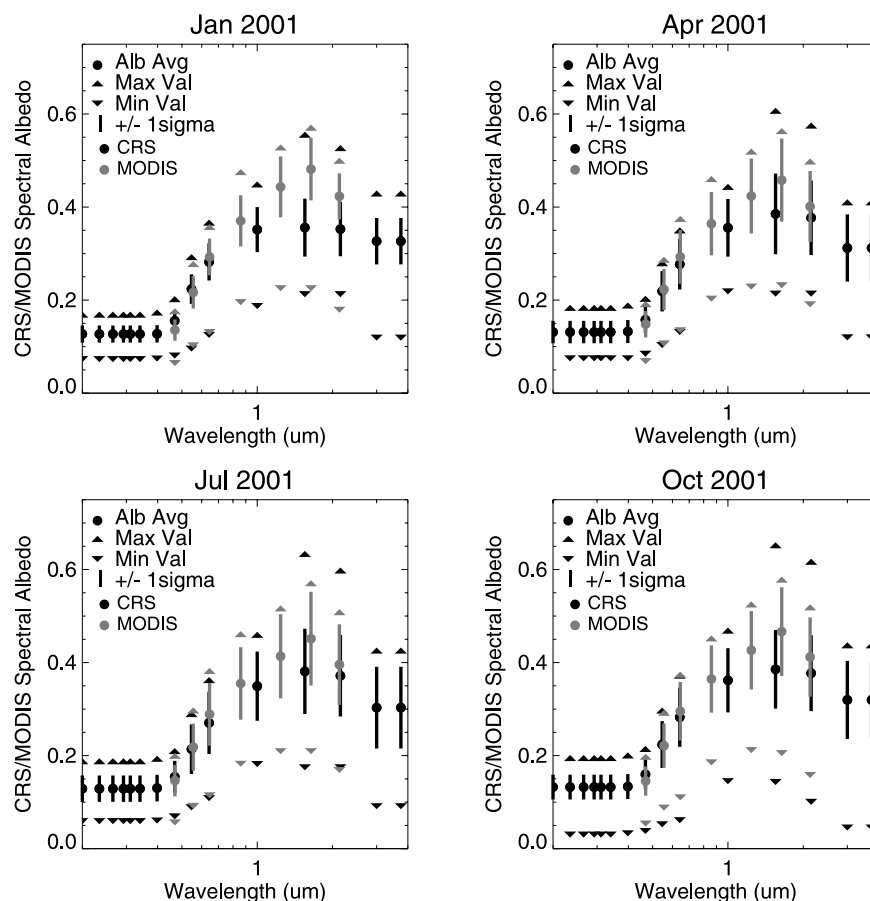
Figure 16. Desert surface spectral albedo for CRS in 15 Langley Fu and Liou bands (black) and 7 MODIS channels (gray) shown as a mean (solid circles), maximum and minimum values (up/down triangles), and 1 standard deviation for all comparison points (vertical lines).

albedo spectral shape. So the question of how well do the CERES albedo spectral shapes compare to those from the MODIS data product arises? As a gross assessment of a priori spectral shape used by CRS, statistics were compiled as a function of wavelength for the resulting spectral albedos from the footprints in Figures 9 (land) and 12 (desert). These statistics were then plotted; means (solid circles), standard deviations (vertical bars), minimums and maximums (hats), in Figures 15 (land) and 16 (desert). The color gray indicates results from MODIS, black, results from CRS. For all land surface types in Figure 15 we find a fairly good agreement in the shortwave portion of the spectrum below 1 micron in all months with some key differences. In January the 0.63 μm channel is brighter in MODIS than in the CRS average. In fact, the mean CRS value falls near the minimum MODIS value. At the important 0.86 μm channel (band 0.69–1.30 μm for LFL05) means and standard deviations are comparable, but minimum values of CRS are significantly lower than those of MODIS. Mean values match well in April and July, though are lower for CRS in January and October. The comparison is not as good for wavelengths greater than 1.0 micron, where for each month the CRS values underestimate those reported by the MODIS product. These wavelengths contribute to the consistently negative tendency of CRS broadband albedo (compared with MODIS) shown in Figures 9 and 12. Roughly 23% of the solar insolation at the surface is

found at wavelengths above 1.0 μm, for a climatological midlatitude summer at a solar zenith of $60°$. It appears that CRS albedo spectral shapes could be improved by folding in MODIS values. Figure 16 shows the same spectral albedo comparison as Figure 15 but for four desert sites whose broadband albedo comparison is found in Figure 12. As desert scenes tend to simpler spectral shape, these comparisons match slightly better than those for the land scenes. Below 1 micron the comparison is quite good however, again for wavelengths greater than 1 micron the CERES CRS spectral shapes underestimate the mean values found at the desert sites by the MODIS albedos.

7. Conclusions

[43] We have described in detail the methodology for deriving clear and cloudy sky broadband albedo and spectral shape for use, globally; by applying the radiation transfer routines used in CERES/SARB subsystem that produces the Clouds and Radiation Swath (CRS) data product. The importance of accurately defining spectral surface albedo is justified due to the impact of the interaction of aerosols and albedo with respect to the forcing of SW flux at the top of the atmosphere. For clear sky footprints the methodology is assessed against an independent product from the higher spectral resolution MODIS instrument on board the same EOS Terra satellite. Comparisons of

the CERES CRS surface albedo to surface observed albedos from radiometers mounted at 10 m are untenable. Instead, as encouraged by the CEOS/WGCV/LPV Albedo Subgroup, we integrate MODIS BRDF based albedos into the CERES footprints and compare these integrated values against the ratio of the upward to downward fluxes as calculated by the SARB code. Matching these independent products in space and time, and weighting the MODIS according to an approximation of the energy response of the CERES instrument, shows significantly improved results over comparisons with albedo observed from instruments mounted on 10-m towers as found in Figure 5. Over land sites, mean difference for all footprint comparisons are −0.004 absolute, or 2.4% relative to the MODIS product means. RMS also remains small from 0.015 to 0.020 depending on month. These values of RMS are approximately 10% relative to the MODIS albedo mean.

[44] When only the more homogeneous desert footprints are considered, absolute bias remains approximately the same at −0.006. However, mean albedo and mean solar zenith angle for these latitudes also increase and the relative bias with respect to mean MODIS albedo actually drops to 2.1%. Mean RMS for the four desert months/footprints considered is approximately 0.02 or less than 10% of the MODIS mean albedo.

[45] For both desert and land scene types, for all months, we find the difference between the two albedo products increases as aerosol optical depth increases. There was some dependence in desert scenes of the albedos on VZA of the CERES instruments as well as a slight positive slope dependence of the desert albedos on SZA. These dependencies tend to cancel in the mean. A comparison of spectral shapes, based on a gross average of all footprints for the two clear sky scene types, determined that in general the two products match better in the shorter wavelengths than for those above 1 micron.

[46] Each large, clear CERES CRS footprint over land has its own retrieval for surface albedo. The CRS product for land surface albedo at Terra overpass appears to be reasonably accurate but rather noisy with input for AOD as a principal source of the noise. A comparison with MODIS retrievals and ground-based observations indicates CRS surface albedos tend to have a low bias. Filtering based on AOD may be the way to a produce a more useful monthly CRS surface albedo. Succeeding generations of CERES data products for surface albedo may be more useful for calculation of aerosol forcing by incorporating information on spectral albedo from the MODIS Land Team.

References

Augustine, J. A., J. J. DeLuisi, and C. N. Long (2000), SURFRAD – A National Surface Radiation Budget Network for Atmospheric Research, *Bull. Am. Meteorol. Soc.*, *81*(10), 2341–2358.

Bacour, C., and F.-M. Bréon (2005), Variability of biome reflectance directional signatures as seen by POLDER, *Remote Sens. Environ.*, *98*, 80–95, doi:10.1016/j.rse.2005.06.008.

Barkstrom, B. R., and G. L. Smith (1986), The Earth radiation budget experiment: Science and implementation, *Rev. Geophys.*, *24*, 379–390.

Betts, R. A., P. D. Fallon, K. K. Goldewijk, and N. Ramankutty (2007), Biogeophysical effects of land use on climate: Model simulations of radiative forcing and large-scale temperature change, *J. Agric. For. Meteorol.*, *142*(2–4), 216–233.

Bicheron, P., and M. Leroy (2000), Bidirectional reflectance distribution function signatures of major biomes observed from space, *J. Geophys. Res.*, *105*, 26,669–26,681.

Bloom, S., et al. (2005), Documentation and Validation of the Goddard Earth Observing System (GEOS) Data Assimilation System - Version 4, *Tech. Rep. Series on Global Modeling and Data Assimilation 104606*, 26. (Available at http://gmao.gsfc.nasa.gov/systems/geos4/)

Briegleb, B. P., and V. Ramanathan (1982), Spectral and diurnal variations in clear sky planetary albedo, *J. Appl. Meteorol.*, *21*, 1160–1171.

Briegleb, B. P., P. Minnis, V. Ramanathan, and E. Harrison (1986), Comparison of regional clear-sky albedos inferred from satellite observations and models comparisons, *J. Clim. Appl. Meteorol.*, *25*, 214–226.

Charlock, T. P., F. G. Rose, D. A. Rutan, T. A. Alberta, D. P. Kratz, L. H. Coleman, G. L. Smith, N. M. Smith, and T. D. Bess (1997), Clouds and the Earth's Radiant Energy System (CERES) algorithm theoretical basis document: Compute surface and atmospheric fluxes (subsystem 5). (Available at http://science.larc.nasa.gov/ceres/ATBD/)

Charlock, T. P., F. G. Rose, D. A. Rutan, Z. Jin, and S. Kato (2006), The global surface and atmosphere radiation budget: An assessment of accuracy with 5 years of calculations and observations, paper presented at 12th Conference on Atmospheric Radiation (AMS), 10–14 July, Madison, Wis. (Available at http://ams.confex.com/ams/Madison2006/techprogram/programexpanded_345.htm)

Collins, W. D., P. J. Rasch, B. E. Eaton, B. V. Khattatov, J.-F. Lamarque, and C. S. Zender (2001), Simulating aerosols using a chemical transport model with assimilation of satellite aerosol retrievals: Methodology for INDOEX, *J. Geophys. Res.*, *106*, 7313–7336.

Forster, P., et al. (2007), Changes in atmospheric constituents and in radiative forcing, in *Climate Change 2007: The Physical Science Basis. Contribution of Working Group I to the Fourth Assessment Report of the Intergovernmental Panel on Climate Change*, edited by S. Solomon, et al., pp. 129–234, Cambridge Univ. Press, New York.

Fu, Q., and K.-N. Liou (1993), Parameterization of the radiative properties of cirrus clouds, *J. Atmos. Sci.*, *50*, 2008–2025.

Gao, F., C. B. Schaaf, A. H. Strahler, A. Roesch, W. Lucht, and R. Dickinson (2005), MODIS bi-directional reflectance distribution function and albedo climate modeling grid products and the variability of albedo for major global vegetation types, *J. Geophys. Res.*, *110*, D01104, doi:10.1029/2004JD005190.

Geiger, B., O. Samain, F. Baret, O. Hagolle, P. Bicheron, J.-L. Roujean, L. Franchisteguy, and M. Leroy (2004), Multi-sensor data fusion for deriving bio-physical variables in the Cyclopes project, in *Geoscience and Remote Sensing Symposium, IGARSS '04. Proceedings*, *4*, 2524–2527.

Green, R., and B. A. Wielicki (1997), Clouds and the Earth's Radiant Energy System (CERES) Algorithm Theoretical Basis Document: Convolution of imager cloud properties with CERES footprint point spread function (Subsystem 4.4). (Available at http://science.larc.nasa.gov/ceres/ATBD/)

Gupta, S. K., D. P. Kratz, P. W. Stackhouse, and A. C. Wilber (2001), The Langley parameterized shortwave algorithm (LPSA) for surface radiation budget studies, *NASA TP 2002-211272*, 31 pp.

Hautecœur, O., and M. Leroy (1998), Surface bidirectional reflectance distribution function observed at global scale by POLDER/ADEOS, *Geophys. Res. Lett.*, *25*, 4197–4200.

Hess, M., P. Koepke, and I. Schult (1998), Optical properties of aerosols and clouds: The software package OPAC, *Bull. Am. Meteorol. Soc.*, *79*, 831–844.

Jin, Z., K. Stamnes, W. F. Weeks, and S. C. Tsay (1994), The effects of sea ice on the solar energy budget in the atmosphere-sea ice-ocean system: A model study, *J. Geophys. Res.*, *99*, 25,281–25,294.

Jin, Y., C. B. Schaaf, C. E. Woodcock, F. Gao, X. Li, A. H. Strahler, W. Lucht, and S. Liang (2003), Consistency of MODIS surface bidirectional reflectance distribution function and albedo retrievals: 2. Validation, *J. Geophys. Res.*, *108*(D5), 4159, doi:10.1029/2002JD002804.

Jin, Z., T. P. Charlock, W. L. Smith, and K. Rutledge (2004), A parameterization of ocean surface albedo, *Geophys. Res. Lett.*, *31*, L22301, doi:10.1029/2004GL021180.

Jin, Z., T. P. Charlock, K. Rutledge, G. Cota, R. Kahn, J. Redemann, T. Zhang, D. A. Rutan, and F. Rose (2005), Radiative transfer modeling for the CLAMS experiment, *J. Atmos. Sci.*, *62*, 1053–1071.

Jin, Z., T. P. Charlock, P. Yang, S. R. Hudson, and S. G. Warren (2008), Snow optical properties for different particle shapes with application to snow grain size retrieval and MODIS/CERES radiance simulation over Antarctic, *Remote Sens. Environ.*, *112*, 3563–3581.

Kato, S., F. G. Rose, and T. P. Charlock (2005), Computation of domain-averaged irradiance using satellite-derived cloud properties, *J. Atmos. Ocean. Technol.*, *22b*, 146–164.

Liang, S., A. H. Strahler, and C. W. Walthall (1999), Retrieval of land surface albedo from satellite observations: A simulation study, *J. Appl. Meteorol.*, *38*, 712–725.

Loeb, N. G., S. Kato, K. Loukachine, and N. Manalo-Smith (2005), Angular distribution models for top-of-atmosphere radiative flux estimation from the Clouds and the Earth's Radiant Energy System on the Terra satellite. part I: Methodology, *J. Atmos. Ocean. Technol.*, *22*, 338–351.

Loeb, N. G., S. Kato, K. Loukachine, N. Manalo-Smith, and D. R. Doelling (2007), Angular distribution models for top-of-atmosphere radiative flux estimation from the Clouds and the Earth's Radiant Energy System on the Terra satellite. part II: Validation, *J. Atmos. Ocean. Technol.*, *22*, 338–351.

Long, C. N., and T. P. Ackerman (2000), Identification of clear skies from broadband pyranometer measurements and calculation of downwelling shortwave cloud effects, *J. Geophys. Res.*, *105*, 15,609–15,626.

Lucht, W., C. B. Schaaf, and A. H. Strahler (2000b), An algorithm for the retrieval of albedo from space using semi-empirical BRDF models, *IEEE Trans. Geosci. Remote Sens.*, *38*, 977–998.

Maignan, F., F.-M. Breon, and R. Lacaze (2004), Bidirectional reflectance of Earth targets: Evaluation of analytical models using a large set of spaceborne measurements with emphasis on the hot spot, *Remote Sens. Environ.*, *90*, 210–220.

Minnis, P., D. F. Young, S. Sun-Mack, P. W. Heck, D. R. Doelling, and Q. Trepte (2003), CERES cloud property retrievals from imagers on TRMM, Terra, and Aqua, in *Remote Sensing of Clouds and the Atmosphere VIII*, edited by K. P. Schaefer et al., Int. Soc. for Opt. Eng., *SPIE Proc.*, *5235*, 37–48.

Minnis, P., D. F. Young, S. Sun-Mack, Q. Z. Trepte, R. R. Brown, S. Gibson, and P. Heck (2004), Diurnal, seasonal, and interannual variations of cloud properties derived for CERES from imager data [CD-ROM], in *Proc. of the Thirteenth American Meteorological Society Conference Satellite Oceanography and Meteorology*, Norfolk, Va., 20–24 Sept., P6.10.

Myers, D. R., S. Wilcox, M. Anderberg, S. H. Alawaji, N. M. Al Abbadi, and M. Y. bin Mahfoodh (1999), Saudi Arabian solar radiation network of data for validating satellite remote-sensing systems, in *Earth Obs. Sys. IV SPIE*, vol. 3750, edited by W. L. Barnes, 18–20 July, Denver, Colo. (Available at http://spie.org/x1848.xml)

Ohmura, A., et al. (1998), Baseline Surface Radiation Network (BSRN/WCRP): New precision radiometry for climate change research, *Bull. Am. Meteorol. Soc.*, *79*(10), 2115–2136.

Pinker, R. T., and A. Karnieli (1995), Characteristic spectral reflectance of a semi-arid environment, *Int. J. Remote Sens.*, RS100424.

Pinker, R. T., and I. Laszlo (1992), Modeling of surface solar irradiance for satellite applications on a global scale, *J. Appl. Meteorol.*, *31*, 195–211.

Remer, L. A., et al. (2005), The MODIS aerosol algorithm, products, and validation, *J. Atmos. Sci.*, *62*, 947–973.

Roesch, A., C. Schaaf, and F. Gao (2004), Use of moderate-resolution imaging spectroradiometer bi-directional reflectance distribution function products to enhance simulated surface albedo, *J. Geophys. Res.*, *109*, D12105, doi:10.1029/2004JD004552.

Rose, F. G., and T. P. Charlock (2002), New Fu-Liou Code Tested with ARM Raman Lidar and CERES in pre-CALIPSO Exercise, Extended abstract for *11th Conference on Atmospheric Radiation (AMS)*, 3–7 June, Ogden, Utah.

Rutan, D., T. Charlock, F. Rose, S. Kato, S. Zentz, and L. Coleman (2006), Global Surface Albedo from CERES/TERRA Surface and Atmospheric Radiation Budget (SARB) Data Product, in *Proceedings of 12th Conference on Atmospheric Radiation (AMS)*, 10–14 July 2006, Madison, Wis. (Available at http://ams.confex.com/ams/Madison2006/techprogram/programexpanded_345.htm)

Salomon, J. G., A. H. Strahler, F. Gao, and Y. Jin (2006), Validation of the MODIS bi-directional reflectance distribution function and albedo retrievals using combined observation from the Aqua and Terra platforms, *IEEE Trans. Geosci. Remote Sens.*, *44*(6), 1555–1564.

Schaaf, C. B., et al. (2002), First operational BRDF albedo nadir reflectance products from MODIS, *Remote Sens. Environ.*, *83*, 135–148.

Smith, G. L., and R. N. Green (1981), Deconvolution of wide field-of-view radiometer measurements of earth-emitted radiation. part I: Theory, *J. Atmos. Sci.*, *38*, 461–473.

Smith, W. L., Jr., T. P. Charlock, R. Kahn, J. V. Martins, L. A. Remer, P. V. Hobbs, J. Redemann, and C. K. Rutledge (2005), EOS-TERRA aerosol and radiative flux validation: An overview of the Chesapeake Lighthouse and Aircraft Measurements for Satellites (CLAMS) experiment, *J. Atmos. Sci.*, *62*, 903–918.

Suttles, J. T., R. N. Green, P. Minnis, G. L. Smith, W. F. Staylor, B. A. Wielicki, I. J. Walker, D. F. Young, V. R. Taylor, and L. L. Stowe (1988), Angular radiation models for the earth-atmosphere system, vol. I: Shortwave Radiation, *NASA Ref. Publ. RP-1184*, 147 pp.

Tegen, I., and A. A. Lacis (1996), Modeling of particle size distribution and its influence on the radiative properties of mineral dust aerosol, *J. Geophys. Res.*, *101*, 19,237–19,244.

van Leeuwen, W., and J.-L. Roujean (2002), Land surface albedo from the synergistic use of polar (EPS) and geo-stationary (MSG) observing systems: An assessment of physical uncertainties, *Remote Sens. Environ.*, *81*, 273–289.

Wang, Z., X. Zeng, and M. Barlage (2007), Moderate resolution imaging spectroradiometer bidirectional reflectance distribution function-based albedo parameterization for weather and climate models, *J. Geophys. Res.*, *112*, D02103, doi:10.1029/2005JD006736.

Wielicki, B. A., B. R. Barkstrom, E. F. Harrison, R. B. Lee III, G. L. Smith, and J. E. Cooper (1996), Clouds and the Earth's Radiant Energy System (CERES): An earth observing system experiment, *Bull. Am. Meteorol. Soc.*, *77*, 853–868.

Yang, S.-K., S. Zhou, and A. J. Miller (2000), SMOBA: A 3-D daily ozone analysis using SBUV/2 and TOVS measurements. (Available at www.cpc.ncep.noaa.gov/products/stratosphere/SMOBA/smoba_doc.shtml)

Zhou, Y., K. C. Rutledge, T. P. Charlock, N. C. Loeb, and S. Kato (2001), Atmospheric correction using MODTRAN for TOA and surface BRDF characteristics from high resolution spectroradiometeric/angular measurements from helicopter platform, *Adv. Atmos. Sci.*, *18*, 984–1004.

_____

T. Charlock, Science Directorate, NASA Langley Research Center, Mail Stop 420, 21 Langley Boulevard, Room 170, Hampton, VA 23681-2199, USA.

N. Manalo-Smith, F. Rose, and D. Rutan, Science Systems and Applications, Inc., 1 Enterprise Parkway, Suite 200, Hampton, VA 23666, USA. (david.a.rutan@nasa.gov)

M. Roman and C. Schaaf, Department of Geography, Center for Remote Sensing, Boston University, 675 Commonwealth Avenue, Room CAS 436, Boston, MA 02215, USA.